

A DEEP SPITZER SURVEY OF CIRCUMSTELLAR DISKS IN THE YOUNG DOUBLE CLUSTER, h AND χ PERSEI

RYAN CLOUTIER¹, THAYNE CURRIE¹, GEORGE H. RIEKE², SCOTT J. KENYON³, ZOLTAN BALOG⁴, RAY JAYAWARDHANA^{1,5}

Draft version August 11, 2014

ABSTRACT

We analyze very deep IRAC and MIPS photometry of $\sim 12,500$ members of the 14 Myr old Double Cluster, h and χ Persei, building upon on our earlier, shallower Spitzer Cycle 1 studies (Currie et al. 2007, Currie et al. 2008). Numerous likely members show infrared (IR) excesses at $8\ \mu\text{m}$ and $24\ \mu\text{m}$ indicative of circumstellar dust. The frequency of stars with $8\ \mu\text{m}$ excess is at least 2% for our entire sample, slightly lower (higher) for B/A stars (later type, lower-mass stars). Optical spectroscopy also identifies gas in about 2 % of systems but with no clear trend between the presence of dust and gas. Spectral energy distribution (SED) modeling of 18 sources with detections at optical wavelengths through MIPS $24\ \mu\text{m}$ reveals a diverse set of disk evolutionary states, including a high fraction of transitional disks, although similar data for all disk-bearing members would provide constraints. Using Monte Carlo simulations, we combine our results with those for other young clusters to study the global evolution of dust/gas disks. For nominal cluster ages, the e-folding times (τ_0) for the frequency of warm dust and gas are 2.75 Myr and 1.75 Myr respectively. Assuming a revised set of ages for some clusters (e.g. Bell et al. 2013), these timescales increase to 5.75 and 3.75 Myr, respectively, implying a significantly longer typical protoplanetary disk lifetime than previously thought. In both cases the transitional disk duration, averaged over multiple evolutionary pathways, is $\approx 1\ \text{Myr}$. Finally, $24\ \mu\text{m}$ excess frequencies for 4–6 M_\odot stars appear lower than for 1–2.5 M_\odot stars in other 10–30 Myr old clusters.

1. INTRODUCTION

Planet formation around other stars provides a reference point for understanding the formation and early evolution of the solar system. Nearly all stars are born surrounded by optically thick disks of gas and dust (Adams et al. 1987; Strom et al. 1989; Hernandez et al. 2007a; Gutermuth et al. 2009), which comprise the building blocks of planets. Over time, dust grains in these protoplanetary disks settle towards the mid-plane and coagulate into larger, lower-opacity bodies (Dullemond & Dominik 2005). Protoplanetary disk gas (and dust entrained in it) is drained by accretion onto the star (Hartmann et al. 1998). Hence, the frequency of detectable gas-rich dusty protoplanetary disks decreases with time (Hernandez et al. 2007a; Currie and Sicilia-Aguilar 2011).

By 10–20 Myr, the frequency of gas-rich dusty disks has dropped effectively to zero. Few stars show infrared broadband excess consistent with warm, optically thick protoplanetary disk dust (Silverstone et al. 2006; Currie et al. 2007a), cold gas from outer disk regions (Pascucci et al. 2006; Dent et al. 2013), or accreting gas from inner disk regions (Jayawardhana et al. 2006; Fedele et al. 2010). Optically-thin, gas poor debris disks have second-generation dust originating from planetesimal collisions (Wyatt 2008; Kenyon and Bromley 2008). They comprise most of the disk population at ages beyond 10 Myr (Rieke et al. 2005; Su et al. 2006;

Carpenter et al. 2009a) and first emerge around stars nominally age-dated to 3–5 Myr (Carpenter et al. 2006; Currie et al. 2009; Currie & Kenyon 2009).

Stars with ages of several Myr to 10–20 Myr, therefore, clarify the timescale for and probe the structures of dissipating protoplanetary disks and the transition from these disks to debris disks. Most recent studies suggest an e-folding timescale of ~ 3 Myr for protoplanetary disk dust and gas (Hernandez et al. 2007a; Fedele et al. 2010; Currie and Sicilia-Aguilar 2011). Fewer than $\sim 20\%$ of such disks around stars of solar mass or greater remain at ~ 5 Myr (Currie et al. 2009; Currie & Kenyon 2009).

The morphologies of protoplanetary disks at these intermediate ages also show evidence for significant evolution. Fewer disks have optically thick at all IR wavelengths, characteristic of nearly all Myr-old “primordial” disks. More disk exhibit reduced IR emission, consistent with inner disk clearing. As shown by SED modeling, many of these transitional protoplanetary disks have an optically thin *inner hole/cavity* that retain an optically thick outer disk (Calvet et al. 2005; Espaillat et al. 2007). Many other disks exhibit a reduced luminosity at IR to submm wavelengths and likely represent a second evolutionary pathway, *homologously depleted* transitional disks (Currie et al. 2009), although this population is challenging to distinguish from some primordial disks with dust settling (Luhman et al. 2010; Currie and Sicilia-Aguilar 2011). Nevertheless, the relatively high frequency of the combined transitional disk population suggests that this phase, averaged over all pathways, comprises an appreciable fraction (e.g. 30%) of the total disk lifetime (Currie et al. 2009; Currie and Sicilia-Aguilar 2011), although the exact sizes of the transitional disk populations and relative lifetimes for different morphologies are still be-

cloutier@cita.utoronto.ca, currie@astro.utoronto.ca, griek@as.arizona.edu, skenyon@cfa.harvard.edu

¹ University of Toronto., 50 St. George St., Toronto, ON

² Steward Observatory, University of Arizona

³ Harvard-Smithsonian Center for Astrophysics, 60 Garden St. Cambridge, MA 02140

⁴ Max Planck Institute for Astrophysics-Heidelberg

⁵ Department of Physics and Astronomy, York University

ing debated (Muzerolle et al. 2010; Luhman et al. 2010; Currie and Sicilia-Aguilar 2011; Espaillat et al. 2014).

However, our understanding of protoplanetary disk and early debris disk evolution hinges on key, recently challenged assumptions about the samples comprising the above mentioned studies. In particular, while the relative ages of young clusters can be reliably determined, absolute ages are highly uncertain (see discussion in Soderblom et al. 2014). Bell et al. (2013) and Peca et al. (2012) find that stars in many clusters nominally age-dated to 2-5 Myr and used to derive disk evolution timescales are about twice their nominal age. However, studies deriving the protoplanetary disk timescale and the transitional disk duration generally assume nominal, systematically younger ages (Hernandez et al. 2007a; Currie and Sicilia-Aguilar 2011).

Moreover, our knowledge about disk evolution is limited by poor constraints on the properties of disks around some kinds of stars at 10-20 Myr. Few protoplanetary disks remain around any stars age-dated at ~ 10 -20 Myr. Ensembles of such disks much larger than the populations of nearby clusters are needed to investigate the morphologies and relative frequency of the longest-lived protoplanetary disks. While planets appear around stars as massive as $4.5 M_{\odot}$ (Hatzes et al. 2005), studies focused on nearby clusters have only explored the disk populations around $M \lesssim 2.3 M_{\odot}$ (e.g. late B/early A type) stars. For any reasonable initial mass function (e.g. Miller & Scalo 1979), these massive stars are far less frequent than the AFGKM stars normally analyzed in disk evolution surveys. Therefore extremely populous clusters at 10-20 Myr are required to investigate statistically the last vestiges of the protoplanetary disk phase and complete our understanding of the frequencies of debris disks around all types of planet-bearing stars.

The massive 14 Myr old Double Cluster, η and χ Persei, provides us with a valuable laboratory for studying disk evolution at 10-20 Myr. The large population of stars ($\sim 12,500$) in this region at a wide range of evolutionary states allows us to constrain the frequency and morphologies of the longest-lived protoplanetary disks. Additionally, η and χ Persei contains a large number of very early type, massive stars ($\text{SpT} \lesssim \text{B6}$, $M \geq 4 M_{\odot}$) relative to other nearby clusters, allowing us to investigate the disk populations of the most massive stars. Lastly, compared to most other clusters, the age of η and χ Persei is well constrained. A number of independent diagnostics such as pre-main-sequence isochrones, the main-sequence turnoff, and the luminosity of M supergiants (Slesnick et al. 2002; Currie et al. 2010; Bell et al. 2013) independently point to an age of 14 Myr. Because the derived disk lifetimes are dependent on cluster age, precise knowledge of the age of η and χ Persei helps to clarify the protoplanetary disk lifetime as well as the relative frequency and morphology of long-lasting protoplanetary disks.

Previous *Spitzer Space Telescope* data for η and χ Per provide a first but very limited probe of the Double Cluster's disk population (Currie et al. 2007a,b, 2008a). IRAC 3.6–8 μm data revealed many stars on the field with red colors consistent with disk emission but was too shallow to detect the photospheres of stars less massive than about $1.3 M_{\odot}$. MIPS-24 μm data identified many large-excess sources consistent with a plateau/peak

in debris emission at 10–20 Myr for (some) stars more massive than the Sun due to icy debris disk evolution, which was verified by analyzing MIPS excesses in nearby regions also found in other studies (Currie et al. 2008a; Hernandez et al. 2007a; Chen et al. 2011). However, these data detected just 17 stars less than $3 M_{\odot}$ with the most luminous debris emission and could not probe the photospheres of the most massive planet-bearing stars. Finally, at the time of these publications, membership lists for the Double Cluster were limited to post-main sequence stars, Be stars, and the most massive main sequence stars (e.g. Slesnick et al. 2002). The candidate member list from Currie et al. (2010) extending η and χ Per's census to subsolar-mass stars was not yet available: warm dust and gas frequencies derived from Currie et al. (2007a,c) are then prone to uncertainties due to contamination from non-members.

In this study we present a deep photometric, infrared study of η and χ Persei members using new *IRAC* and MIPS data from *Spitzer* and the membership list from Currie et al. (2010). The paper is organized as follows: in §2 we describe our data reduction techniques and quantify our completeness limits for both the *IRAC* and MIPS data. In §3 we identify and quantify the frequency of stars surrounded by warm and slightly cooler circumstellar dust while §4 details a similar analysis of gas-rich disks. To further investigate the morphologies of disks around η and χ Persei stars, we then compare the SEDs of members with 8 μm and 24 μm excess to fiducial models representing a range of disk evolutionary states (§5). In §6, we combine our results with those for other clusters to constrain the lifetime of protoplanetary disks and the duration of the transitional disk phase. We conclude with a summary of our results, contrast them with other recent studies, and identify future work that can further constrain the η and χ Persei disk population and clarify key aspects of protoplanetary disk evolution in §7.

2. DATA

2.1. IRAC 3.6–8 μm Data

The Infrared Array Camera (*IRAC*; Fazio et al. 2004) observed η and χ Persei on October 30, 2008 (AOR IDs 2182740, 21828608, 21828096, 21828864, 21828352, and 2182912). Solar activity was normal to below-average. Zodiacal emission ranged between ~ 0.02 and 2 MJy sr^{-1} from 3.6 μm to 8 μm . Image processing and photometry were performed separately for the short exposure and long exposure frames.

2.1.1. Image Processing and Photometry for Short Exposure Data

The short-exposure (0.6 s) *corrected BCD* (Basic Calibration Data; Cbcd) frames have very low source density, no diffuse mid-IR emission (e.g. nebosity), and extremely few residual cosmic ray hits. We processed these data using *MOPEX* (Makovoz et al. 2005), applying an overlap correction and mosaicing the images. Photometry was performed using *PhotVis* (Gutermuth et al. 2004), a slightly-modified GUI-based adaption of the standard IDLPHOT aperture photometry package. We used a 2-pixel ($2''/4$) radius aperture, a sky annulus ranging between 2 and 6 pixels in radius, and the aperture corrections listed in the *IRAC* data handbook.

2.1.2. Image Processing and Photometry for Long Exposure Data

The source density for long exposure data is significantly higher; the long exposure data identify far more stars, including numerous AFGKM cluster members that are too faint ($m[\text{IRAC}] \gtrsim 13$) to be detected by the 0.6s exposures (see Currie et al. 2007a; Currie 2008). To optimize our photometry and thus better insulate our results against photometric uncertainties, we adopt a more detailed approach to image processing and photometry.

Briefly, we first applied the *Array-dependent Pixel Response* correction (Quijada et al. 2004) to each CBCD frame and then mosaic the CBCD frames using MOPEX⁶. We applied an overlap correction to each frame, masking pixels containing bright point sources and calculating each frame's zero-point offset using iterative 3σ clipping to determine the frame's background level.

To determine the distribution of pixel values for each position on the final mosaic, we interpolated values from individual frames using the *drizzle* algorithm with a "drizzle factor" of 0.1. Though very computationally expensive, the *drizzle* algorithm produced the most sharply defined point sources and did not introduce low-frequency pattern noise like that produced by bicubic interpolation. Outlier rejection was performed using the mosaic outlier and *rmask mosaic* modules. Final flux densities for each pixel were derived from the average value of the sigma-clipped stack of pixel values.

For photometry, we use a slightly modified version of the IDLPHOT aperture photometry package, improving the sky background determination, centroiding, and photometric error determination. To identify point sources, we set the detection threshold in each filter in the find.pro routine equal to three times the measured dispersion in the sky background ($\sim 3\sigma_{rms,avg}$). We apply pixel masks on the mosaic to remove the central pixels of all stars and the wings of bright stars from sky background determination. The adopted sky background is set to the median value, not the "mode". As with the short-exposure data, we adopt a two-pixel aperture, a 2–6 pixel sky annulus, and the aperture corrections from the IRAC data handbook. From the uncertainty in the sky background, photon noise, and read noise, we determine the photometric uncertainty, following Currie et al. (2008b).

To select a final list of IRAC detections, we compared lists from the long and short exposure data. For sources brighter than magnitude 10.5 in the long exposure data, we replaced the entries with those from the short exposure data due to saturation (see also Currie et al. 2008b). By matching our catalog to the 2MASS All Sky Survey catalog, we fine-tuned the IRAC data astrometry and produce a combined list of IRAC sources with and without 2MASS counterparts. In all band merging between the IRAC channels and IRAC to MIPS/2MASS etc. we adopted a matching radius of $1''$.

Figure 1 shows a color mosaic image produced from the

⁶ We also tested the artifact mitigation routines described in Currie et al. (2008b) to the "uncorrected" BCD frames. These routines also removed image artifacts (e.g. column pull-down, *muxstripping*), though they did not improve upon corrections from pipeline scripts. To make our results easier to reproduce, we simply used the CBCD frames.

IRAC [3.6], [4.5] and [8] filters (blue, green, and red).

2.1.3. IRAC Source Counts and Detection Limits

Figure 2 shows the distribution of IRAC magnitudes vs. photometric uncertainties. Most sources follow a thin distribution in photometric uncertainty over the full range of magnitudes. However, for each filter a second, sparser distribution lies on top of the main one; many sources have photometric uncertainties $\gtrsim 0.1$ – 0.2 mags even though the errors from photon noise can be $\lesssim 0.05$ mags. Typically, these sources are located in regions of higher stellar density or near the PSF wings of bright stars, so estimates of the local background flux are more uncertain.

Figure 3 displays the number counts in each IRAC band as a function of magnitude. In total, we detect $\sim 110,000$, $\sim 120,000$, $\sim 58,000$, and $\sim 32,500$ candidate point sources in the [3.6], [4.5], [5.8], and [8] filters, respectively. Of these, $\sim 76,000$; $\sim 68,000$; $\sim 31,000$; and $\sim 23,000$ are detected at the 5σ level (dashed line). Because they have matches in multiple IRAC or 2MASS filters, the vast majority of the candidate detections are confirmed: $\sim 80,000$ in [3.6], $\sim 80,000$ in [4.5], $\sim 34,000$ in [5.8], and $\sim 21,000$ in [8].

Compared to the data presented in Currie et al. (2007a, vertical grey lines), our new data are ~ 1.5 – 3 magnitudes deeper in each filter, clearly probing far deeper down the cluster mass function and detecting fainter background sources. The number counts peak at [3.6] ~ 18 , [4.5] ~ 17.8 , [5.8] ~ 16.5 , and [8] ~ 15.5 . Both the distribution of 5σ candidate detections and confirmed detections peak at substantially fainter limits.

2.2. MIPS $24\mu\text{m}$ Data

2.2.1. Image Processing and Photometry

The Multiband Imaging Photometer for Spitzer (MIPS, Rieke et al. 2004) imaged η and χ Persei on March 15–16, 2008, October 25–26, 2008 and March 26 and 29, 2009 as a part of General Observation Programs 40690 and 50664 (PI: Scott Kenyon). The program 40690 observations were focused on the cluster dominated regions with a typical integration time per pixel of 2000s, while the program 50664 data imaged the low-density halo regions surrounding the η Persei and χ Persei centers with a typical integration time per pixel of 1000s. Combined, these observations provide MIPS $24\mu\text{m}$ data for point-sources over a ~ 0.4 square-degree area, covering the core-dominated membership population and much of the known halo population.

Using the Data Analysis Tool (DAT) pipeline, we processed individual BCD frames, removing latent image artifacts and bad pixels, and mosaiced the data using standard outlier rejection similar to that used in the MOPEX reductions of our IRAC data. For point-source detection, we selected groups of pixels lying $> 5\sigma$ above the local background on the mosaic. Point-spread function (PSF) fitting photometry was performed on detected sources on the mosaiced data using model PSFs from the *Spitzer Science Center* webpage.

2.2.2. MIPS Source Counts and Detection Limits

The MIPS data contain 7583 point sources. Of these, 6174 are detected at a 5σ significance or better; 1098

(4270) have counterparts in the 2MASS (IRAC) data. The distribution of $[24]$ vs. $\sigma([24])$ is thicker than for the IRAC bands, largely due to the different survey depth from the two observing programs (Figure 4, left panel). The MIPS source counts peak at $[24] \sim 11.25$ for the shallower program 50664 data, while the deeper program 40690 data yield $5\text{-}\sigma$ detections about a magnitude fainter in regions near the cluster centers. Compared to the MIPS data presented in Currie et al. (2008a) (vertical grey line), our new data are then 0.75–1.75 mags deeper.

2.3. IRAC and MIPS Colors of All Detected Sources

Figure 5 displays the IRAC and MIPS colors for all targets detected in multiple bandpasses with photometric uncertainties less than 0.2 mags ($\sim 5\text{-}\sigma$). Our sample includes a well-defined distribution of objects centered on zero $[3.6]\text{--}[8]$ color (top-left panel), which widens from about 0.1 mag to 0.5–0.75 mag from $[8] = 12$ to $[8] = 15.5$. Our sample also includes a large population of objects with very red $[3.6]\text{--}[8]$ colors ($\gtrsim 1.5$) consistent with those expected for young stellar objects or red, active galaxies (i.e. Gutermuth et al. 2008, 2009, see Appendix of this work). The $[8]$ vs. $[3.6]\text{--}[8]$ diagram also shows a smaller population of objects slightly redder ($[3.6]\text{--}[8] \sim 0.25\text{--}1.5$) than the main distribution of zero-color objects, consistent with the colors expected for highly reddened background stars; red, cool giants; Be stars; and pre-main sequence stars with optically-thin emission from remnant protoplanetary disks or warm debris disks (Currie et al. 2008a; Currie and Sicilia-Aguilar 2011; Kenyon and Bromley 2004). The sample’s distribution of $[24]$ vs. $[3.6]\text{--}[24]$ colors reveals the same kind of populations: objects with zero color, many with very red ($[3.6]\text{--}[24] \gtrsim 4.5$) MIPS colors, and a much smaller population of slightly red objects ($[3.6]\text{--}[24] \sim 0.5\text{--}4.5$).

The bottom panels of Figure 5 clarify the nature of the many objects with strong IRAC/MIPS excesses and the few with weaker excesses. The objects with strong excesses in one band (IRAC or MIPS) must in general be extremely red from $1\text{ }\mu\text{m}$ to $24\text{ }\mu\text{m}$, given the dense clustering of objects at $[3.6]\text{--}[8,24] \sim [1.25,5]\text{--}[2,6]$ (bottom-left panel); the bottom-right panels shows that these red objects preferentially have very faint J -band magnitudes. These colors are consistent with those either for young stellar objects or for active galaxies. Most of the objects with weaker $24\text{ }\mu\text{m}$ excesses appear to have very weak to negligible IRAC excesses, concentrated mainly along a narrow band from $[3.6]\text{--}[8,24] \sim [0,0.5]$ to $[0.5,4.5]$, and have $J \sim 12.5\text{--}16.5$, comparable to the near-IR brightnesses of AFGK members in h and χ Persei (Currie et al. 2010).

2.4. Ancillary Data Establishing Cluster Members

To identify and characterize disks surrounding h and χ Persei stars, we combine Spitzer data with optical/near-IR data for likely cluster members, updating the list from Currie et al. (2010) with a more accurate one of 13,956 stars (Table 1)⁷. Optical spectroscopy confirms the stellar nature of sources, provides a better estimate

of the stars’ intrinsic fluxes by yielding their extinctions, and reveals whether the stars show evidence for circumstellar gas accretion, which can be present for protoplanetary disks but is absent for debris disks. In total, 12505 ($\sim 90\%$) of the optically-selected cluster members have matches in our Spitzer data. We briefly review the sources of these ancillary data.

2.4.1. Optical and Near-Infrared Photometry

Optical VI_c photometry of h and χ Persei stars was originally taken as a part of the MONITOR program (Aigrain et al. 2007) and covers ~ 0.6 square degrees on the sky. We supplement this photometry with that from Slesnick et al. (2002), which was a shallower survey covering a wider, ~ 1 square degree area. Cluster stars with optical photometry range in mass from bright, $\sim 15\text{--}20\text{ }M_\odot$ supergiants to very faint, $\sim 0.2\text{ }M_\odot$ pre-main sequence M stars (see Currie et al. 2010).

Near-IR JHK_s band photometry is drawn from the 2MASS All-Sky Survey (Skrutskie et al. 2006). The survey has nominal $10\text{ }\sigma$ limits of $J = 15.8$ and $K_s = 14.3$. However, the number counts of detections in the h and χ Persei field suggest completion limits of $J = 15.5$ and $K_s = 15$ (Currie et al. 2007a), where the formal photometric uncertainties reach ~ 0.1 mags and 0.2 mags, respectively.

2.4.2. Optical Spectroscopy: Identifying Accreting Stars

Finally, we add optical spectroscopy of h and χ Persei stars. The survey presented in Currie et al. (2010) includes $\sim 11,000$ stellar spectra with sufficiently high signal-to-noise to determine accurate spectral types. Currie et al. (2010) limited their membership analysis to spectroscopically-observed stars with V band and 2MASS photometry (7,465), which produced a list of 4,702 members. Many other stars with spectra presented in Currie et al. (2010) but without optical photometry (and thus not analyzed for membership) may in fact be members of the Double Cluster and can be confirmed after obtaining new optical photometry.

Here, we consider evidence for stars accreting gas from protoplanetary disks amongst the entire set of spectra listed in Currie et al. (2010). We derive $EW(H_\alpha)$ with SPTCLASS (Hernandez et al. 2004), which uses the standard IRAF routine *sbands*. Manually comparing $EW(H_\alpha)$ with SPTCLASS-derived estimates for this sample and for the previously reported sample from Currie et al. (2007c) shows excellent agreement.

Based on these measurements, we identify accretors from the subset of spectra not previously analyzed in Currie et al. (2007c) and revisit the Currie et al. (2007c) classifications. The spectra analyzed in Currie et al. (2007c) are largely drawn from 2006 MMT/Hectospec observations focused on χ Persei, the less massive of the

⁷ Specifically, further inspection of the membership list presented in Currie et al. shows that our color-magnitude criteria identifying members from VI photometry at our sensitivity limit ($V \sim 23\text{--}$

24) and/or for the reddest objects ($V\text{--}I \gtrsim 4$) was insufficiently stringent, including some stars lying more than 0.75 mags above the main cluster locus. We also removed several duplicate entries for the brightest stars, which were not previously flagged since their centroid positions from the three optical imaging datasets differed enough that they were not identified as the same source. These steps reduce the number of Double Cluster members by $\sim 1\%$. Note that removing all of these sources has no bearing on the bulk cluster properties (distance, reddening, age) reported in Currie et al. (2010).

two regions of h and χ Persei (see Currie 2008). Thus, newly-identified accretors are mainly drawn from regions surrounding h Persei and the low-density halo population. Our analyses are described in §4.

2.5. Combined Spitzer and Ground-Based Sample Characteristics

2.5.1. IRAC and MIPS Completeness

To select point sources with dust emission, we rely on the $8\ \mu\text{m}$ IRAC data and the $24\ \mu\text{m}$ MIPS data. Within the far more sensitive $[3.6]$ and $[4.5]$ IRAC images, we detect nearly all (90%–95%) cluster members from $V \sim 6$ ($[3.6] \sim [4.5] \sim 3\text{--}5$) to $V = 24$ ($[3.6] \sim [4.5] \sim 17\text{--}17.5$). Members lacking detections fall outside of the IRAC coverage. Thus, the ratio of the detection frequencies at $[8]$ ($[24]$) and $[4.5]$ provide a robust estimate of the completeness at $8\ \mu\text{m}$ ($24\ \mu\text{m}$). Figure 8 shows the result.

Figure 8 (top panels) assesses our sample completeness. Our $8\ \mu\text{m}$ completeness diverges from 100% at $V > 17$ and drops below 50% by $V = 22$. Our $24\ \mu\text{m}$ completeness drops from a maximum value of $\sim 80\%$ at $V = 11$ to 25% by $V = 13$. In §4, we derive statistics for disk emission in a given filter only for h and χ Persei stars where we detect at least 25% of the sample. Thus, at $8\ \mu\text{m}$, we focus on stars brighter than $V = 22$. At $24\ \mu\text{m}$, we derive statistics for stars brighter than $V = 13.5$.

The bottom panels of Figure 8 assess the level to which the $5\text{-}\sigma$ cutoff we will impose for analyzing our IRAC detections (Section 3) may bias our results. For stars with $V = 11\text{--}19$, $19\text{--}20$, $20\text{--}21$, and $21\text{--}22$, the typical $[8]$ photometric uncertainties are $\sigma([8]) \approx 0.05\text{--}0.1$, 0.1 , 0.15 , and 0.175 , respectively. For these V magnitude bins, the percentage of stars detected at better than a $5\text{-}\sigma$ level at $[8]$ is 99.5%, 95%, 86.3%, and 76%, respectively. We obtain similar results for V vs. $[24]$ and $\sigma([24])$. For the brightest stars, all MIPS-24 detections are $5\text{-}\sigma$ detections, while the majority of detections near our faint limit ($V = 13.5$) are likewise $5\text{-}\sigma$.

2.5.2. Masses of Spitzer-Detected h and χ Persei stars

Double Cluster members targeted by Spitzer cover a wide range of optical/IR brightnesses, spectral types, and thus stellar masses. To estimate the typical stellar masses corresponding to an h and χ Persei star of a given optical brightness, we use two sets of isochrones – Baraffe et al. (1998) for stars less than $1.4\ M_{\odot}$ and Palla and Stahler (1999) for more massive stars. To map between the stars’ effective temperatures predicted from these isochrones and spectral type and median V -band magnitude, we first adopt the effective temperature scale listed in Currie et al. (2010)⁸. We compute the median V -band magnitude for stars of a given mass/spectral type

⁸ Note that the stellar mass sampling from the Palla and Stahler (1999) isochrones is quite coarse, and thus values for the upper main sequence in h and χ Persei are less precisely determined than for the pre-main sequence. However, we opt to use these isochrones since they yield an age for other young associations – specifically, Upper Scorpius – that can agree with the age derived from Baraffe et al. (1998) (cf. Preibisch et al. 2002). Other isochrones with better sampling may yield spurious stellar mass-dependent age spreads (Currie et al. 2010). Furthermore, while the sampling in mass is coarse, the resultant sampling in spectral type and V -band magnitude is not (see Table 3). We will further discuss stellar ages in §6.

directly for BAF stars since such stars are well sampled from our spectroscopic survey (Currie et al. 2010) and are on/very near the main sequence so the adopted T_{eff} scale should match that of field dwarfs. For lower-mass stars poorly probed by our spectroscopic survey, we simply adopt a distance of $2.34\ \text{kpc}$ and a mean Double Cluster reddening of $E(B\text{--}V) = 0.54$ (derived mostly from BAF stars). From these assumptions, we determine the predicted V -band magnitude for these lower-mass, later-type stars.

Table 3 shows the expected spectral type and V band magnitudes for cluster members with different stellar masses. Stars with $V \approx 12, 13, 15, 18, 19, 20$, and 22 typically have spectral types of $\text{SpT} \approx \text{B2.5}, \text{B4}, \text{A1.5}, \text{K0}, \text{K3}, \text{K5}$, and M1.5 , respectively. Adopting our hybrid Palla & Stahler/Baraffe 14 Myr isochrone to map between spectral type/ T_{eff} and stellar mass, stars with these spectral types typically have stellar masses of $M_{\star} \approx 6, 5, 2, 1.2, 1.1, 0.95$, and $0.6\ M_{\odot}$. Thus, given our IRAC/MIPS completeness limits, we will later only derive the $8\ \mu\text{m}$ excess frequency for stars with $M_{\star} \approx 0.6\text{--}6\ M_{\odot}$ and the $24\ \mu\text{m}$ excess frequency for stars with $M_{\star} \approx 4\text{--}6\ M_{\odot}$ (§3.2 and 3.3).

3. CIRCUMSTELLAR DUST IN DISKS AROUND h & χ PERSEI STARS

Table 2 lists photometry for all $\sim 12,500$ h and χ Persei members with Spitzer data. Here, we first examine the Spitzer colors for cluster members to identify stars with evidence for circumstellar dust. Next, we quantify the frequency of warm dust emission at $8\ \mu\text{m}$ and set limits on the population of members with slightly cooler dust emission probed by MIPS-24 μm data. For all analyses, we restrict our sample to stars with $5\text{-}\sigma$ detections.

3.1. IRAC and MIPS Colors: Evidence for Warm Circumstellar Dust Emission

Figure 6 displays the IRAC/MIPS color-magnitude diagrams for h and χ Persei members. The members-only distributions clearly differ from those of the population of all objects, as they include very few objects with extremely red IRAC and MIPS colors (i.e. $[3.6]\text{--}[8] > 2$, $[3.6]\text{--}[24] > 5$). As shown in the Appendix, the objects with very red colors are most consistent with being PAH-emission galaxies or active galactic nuclei, whereas our members-only sample shares little to no overlap with the range of galaxy colors. There may be some other bona fide, hitherto unidentified cluster members with circumstellar disks amongst our full sample of Spitzer-detected sources. However, focusing only on those objects previously identified as members via optical photometry/spectroscopy allows us to derive statistics on the Double Cluster’s disk population with significantly less extragalactic contamination.

The top panels of Figure 6 show the IRAC $[8]$ vs. $[3.6]\text{--}[8]$ and $[8]$ vs. $[4.5]\text{--}[8]$ distributions for cluster members. The main locus of colors for cluster members is centered roughly about zero with a dispersion that broadens from $\pm 0.05\text{--}0.06$ mags to ~ 0.75 mags for the faintest stars detected at the $5\text{-}\sigma$ level. The distributions exhibit some evidence for a gap in the excess population at $[8] = 11$, where excess sources brighter than this limit all have $[3.6]\text{--}[8] < 0.9$, while fainter excess sources include some with slightly redder colors. Still, the vast majority of

fainter stars with colors redward of the main locus exhibit [3.6]-[8] colors ~ 1 magnitude or less.

To provide a comparison with our sample, we overplot [3.6]-[8] colors typical of blue protoplanetary disks in Taurus from Figure 5 in Luhman et al. (vertical line 2010)⁹. Our sample includes over 10,000 stars and the cluster is only slightly older than clusters/moving groups containing some stars with optically-thick, near-IR luminous disks (e.g. TW Hya, Upper Scorpius). Nevertheless, we identify very few stars whose [3.6]-[8] colors overlap with the range of colors typical for protoplanetary disks. Instead, IRAC excesses for nearly all h and χ Per stars are comparable to the level of emission from the two varieties of transitional disks (Currie et al. 2009; Currie and Sicilia-Aguilar 2011) and warm debris disks indicative of terrestrial planet formation (Kenyon and Bromley 2004; Currie et al. 2007b; Rhee et al. 2007; Lisse et al. 2009).

The MIPS colors (bottom panels) show similar trends. Here, the distributions of [3.6,4.5]-[24] colors broaden from ~ 0.05 magnitudes at the bright end again to a wider distribution for the faintest stars detected at [24]. Stars brighter than 9th magnitude have excesses up to ~ 2 – 2.5 magnitudes. While many stars fainter at [24] likewise exhibit these weak excesses, they also include some with [3.6,4.5]-[24] = 3–5.5, comparable to the 24 μ m excesses exhibited by the most luminous debris disks (Rieke et al. 2005; Low et al. 2005; Currie et al. 2008a) and some transitional disks (Currie and Sicilia-Aguilar 2011). Few stars have [3.6]-[24] colors overlapping with most Taurus stars.

Figure 7 further elucidates the IR excess population for h and χ Persei. As shown in the left-hand panel, most of the stars with 24 μ m excess emission have nearly zero color at [3.6]-[8], though most of the ones with the largest 24 μ m excesses are likewise red at [3.6]-[8]. All of the MIPS-detected stars with [3.6]-[8] excess have clear 24 μ m excess. Thus, there are many more stars with excess at [24] than at [8]; stars with bona fide [8] excesses are virtually certain to have excesses at [24] as well, although they may fall below our [24] detection limit.

The right-hand panel of Figure 7 further demonstrates that for much of our sample we are only identifying the stars with the most luminous 24 μ m excess emission. From the results in Section 2.5, the 24 μ m data only reach the photospheres of B-type stars. Any later-type stars detected in this band must have excess emission.

3.2. IRAC-Excess Emission from Warm Dust

3.2.1. Identifying IRAC-Excess Sources

To identify stars with statistically-significant excess emission at 8 μ m, we follow methods similar to those described in Hernandez et al. (2006) and later work, defining the threshold for an infrared excess source based on the source color compared to the intrinsic dispersion of colors at a given magnitude. The Double Cluster members analyzed here have [8] magnitudes as bright as \sim

⁹ The disagreement between excesses around most Taurus stars and those around h and χ Per stars is even stronger than Figure 6 suggests by eye. Luhman et al. sample includes many stars with excess emission at [3.6] (cf. Hartmann et al. 2005). Few, if any, h and χ Persei stars have excess emission at [3.6] (Currie et al. 2007a). Thus, the 3.6–8 μ m emission for Taurus stars relative to their photospheres is even stronger than h and χ Per’s stars.

5th magnitude and as faint as $\sim [8] = 15.5$, where the former’s photometric errors are negligible and the latter’s are as large as 0.2 magnitudes. While the IRAC colors for young stellar photospheres show little variation for stars earlier than mid-M (cf. Luhman et al. 2010; Pecaute and Mamajek 2013), binarity could in principle artificially redden the system by up to ≈ 0.05 mags (e.g. see Table 13 in Luhman et al. 2010). Additionally, while reddening for most Double Cluster members falls within a range of $E(B-V) = 0.4$ – 0.7 with a median value of 0.52 – 0.56 , Currie et al. (2010) identified some stars best modeled as being far more heavily reddened and some with low reddening. Given various infrared extinction laws (Indebetouw et al. 2005; Flaherty et al. 2007), this range in reddening could induce a spread in color of up to ≈ 0.05 – 0.06 magnitudes in [3.6, 4.5]-[8]. Finally, the IRAC detector also suffers small gain variations across the field depending on whether bright point sources landed on a given pixel in the observations taken immediately prior (Knutson et al. 2007), and small errors in centroiding position due to bright nearby stars may also affect flux and background determinations.

Therefore, instead of defining our threshold for an IR excess source based on intrinsic photometric errors, we empirically derive the spread in photospheric colors and identify excess sources as statistical outliers. For each color-magnitude diagram (e.g. [8] vs. [3.6]-[8]), we first divide the distribution into 0.5 magnitude bins and derive the median color and standard deviation for each bin. We then use a quadratic interpolation to determine the median color and standard deviation at each magnitude. Nominally, we identify $3\text{-}\sigma$ outliers as those with evidence for IR excess. To be conservative, we include an additional 0.06 magnitude buffer to account for color variations due to binarity and differences in reddening, an amount that also roughly corresponds to the spread in IRAC color for the brightest cluster members with negligible photometric errors.

Thus, IR excess sources are defined as those with color $\geq \text{median}(\text{color}) + 3 \times \sigma_{\text{color}} + 0.06$. The empirically-derived dispersion in color is always greater than the quadrature-added uncertainties in the photometric measurements. Compared to the criterion previously used in Currie et al. (2007a), our threshold is less stringent for brighter stars but far stricter for faint stars since it varies as $3 \times \sigma_{\text{empir}}$, not $1 \times \sigma_{\text{phot}}$.

We first compute the frequency of the IRAC-excess population as a function of the stars’ V and I band photometry. We restrict our analysis to stars brighter than $V = 22$, where our completeness drops well below 50% (see §2.5). Furthermore, the percentage of stars whose [8] detections whose high photometric uncertainties ($\sigma([8]) > 0.2$) preclude us from considering them here grows to 14–24% for $V = 20$ – 22 . Therefore, our excess frequencies for the faintest stars ($V = 20$ – 22) are significantly more uncertain than for brighter stars.

Second, we compute the frequency of the IRAC-excess population as a function of the spectral types derived in Currie et al. (2010). Stars with $V \sim 20$ – 22 typically correspond to K5–M1 stars (cf. Table 3). Therefore, only our excess frequencies for stars earlier than mid-K are robust against completeness/photometric biases.

3.2.2. Frequency of IRAC-Excess Sources

Figure 9 shows the frequency of the IRAC-excess population as a function of V , I , and spectral type. Overall, 263 h and χ Persei members or $\sim 2.2\% \pm 0.3\%$ show evidence for 8 μm excess likely due to warm dust. From $V = 14$ to our completeness limits, the frequency of warm dust appears to steadily rise from $\sim 0.5\text{--}1\%$ (e.g. 3/502 and 11/955 at $V = 14\text{--}15$ and $15\text{--}16$, respectively) to $\sim 3\%$ (e.g. 23/843 at $V = 19\text{--}20$) and $\sim 4\text{--}5\%$ (9/193 at $V = 21\text{--}22$). The IRAC excess frequency vs. I shows similar trends. The frequency as a function of spectral type appears roughly flat from A0 to G5 at $\sim 1.5\%$ but rises to 3.5% for K stars, albeit with considerable uncertainty.

If we consider all stars regardless of evolutionary status (black dots in all figure panels), the frequency of warm dust for the brightest stars ($V < 11$, $I < 10$, B0-B5) is as high as in any magnitude/spectral bin covering lower-mass stars. However, many of these stars are known Be stars or other post-main sequence stars whose apparent IRAC excess is likely due to free-free emission or to warm dust from a circumstellar excretion disk and not a circumstellar accretion disk or debris disk connected to planet formation. To estimate the frequency of solely circumstellar disks related to planet formation, we then trim our sample of known Be stars, giants, and supergiants using lists of such stars from Currie et al. (2010), Marsh-Boyer et al. (2012), and from the *SIMBAD* database. In the latter case, various sources contribute to the Be star and (super)giant identifications (Bragg and Kenyon 2005; Slesnick et al. 2002).

The revised IRAC-excess frequencies show that nearly all of the previously-identified excess sources are in fact Be stars or post-main sequence stars. With these stars removed, the excess frequencies for the brightest, earliest stars are $\sim 1\text{--}1.5\%$, comparable to or slightly smaller than their frequencies for slightly fainter, later and (presumably) lower-mass stars ($\sim 1.5\text{--}2\%$). Thus, in agreement with previous results (Currie et al. 2007a; Currie 2008), we identify a slight brightness/spectral-type dependent frequency of warm dust indicating that dusty circumstellar disks are less frequent around the most massive stars ($M \sim 1.5\text{--}5 M_\odot$).

3.3. MIPS-Excess Emission from Cooler Dust

To quantify the frequency of stars with MIPS excesses, we follow the same procedure used in §3.2.1 to flag IRAC excess sources, defining the excess sources as those whose $K_s\text{--}[24]$, $[3.6]\text{--}[24]$, or $[4.5]\text{--}[24]$ colors are redder than the median color by more than $3\text{--}\sigma + 0.06$. Overall, we identify 152 h and χ Persei stars with evidence for excess emission at 24 μm . As explained in Sect. 2.5, we restrict our analysis to stars with $V < 13.5$ due to the poorer MIPS completeness compared to IRAC.

Following §3.2.1, we also derive the frequency in terms of spectral type and mass, using the rough conversion between V magnitude and these two properties as listed in Table 3. Because of poorer sampling in mass and T_{eff} from the Palla and Stahler (1999) isochrones and the large number of post-MS stars dominating spectral types B0 and B1, we restrict the range of spectral types considered to B2–B6. The corresponding mass range is $M_\star = 4\text{--}6 M_\odot$.

Figure 10 displays the frequency of MIPS-24 μm excess emission as a function of V magnitude, spectral type, and mass for these massive, early-type stars. About 5%

of these stars show evidence for MIPS-excess emission from cooler dust compared to the 1–3% that show IRAC excess emission over the same range in V magnitude ($\sim 12\text{--}13.5$), spectral type (\sim mid B), and mass ($4\text{--}6 M_\odot$) (see Figure 9). Although there is a slight decline in excess frequency with increasing V magnitude and later spectral types, the error bars are large enough to easily be consistent with no trend, indicative of a constant frequency of MIPS-excess emission. Any (small) correction for confusion with faint galaxies will not change this conclusion.

4. CIRCUMSTELLAR GAS IN DISKS AROUND h AND χ PERSEI STARS

4.1. Identifying Accreting h and χ Persei Stars

Our criteria for identifying possible accreting systems follows White and Basri (2003)’s spectral-type dependent threshold based on the observed H_α equivalent width. For the stars with spectral types of K0 and later, the $EW(H_\alpha)$ provides a robust measure of accretion (White and Basri 2003). Nominally, for K0–K7 stars, we identify those with $EW(H_\alpha) \geq 3 \text{ \AA}$ as accretors. For K7–M2.5 (M2.5–M5.5) stars, $EW(H_\alpha) \geq 5 \text{ \AA}$ (20 \AA) are flagged as accretors. These criteria are similar to those adopted in Currie & Kenyon (2009) but are more precise than those adopted for h and χ Persei stars in Currie et al. (2007c), where stars with $EW(H_\alpha) > 5\text{--}10 \text{ \AA}$ were identified as candidate accretors.

It is more difficult to identify possible accretors among the AFG-type stars which comprise the bulk of our spectroscopic sample. Within this group of intermediate mass stars, much larger H_α emission line fluxes are required to produce $EW(H_\alpha) > 3 \text{ \AA}$ (e.g. White and Basri 2003). While these stars have additional clear accretion signatures (i.e. U band excess, optical veiling, H_α emission; Calvet et al. 2004), they lack a clear $EW(H_\alpha)$ criterion for separating weakly accreting stars from chromospherically active ones using low-resolution spectroscopy. Because H_α absorption is often much broader than the absorption lines in later-type stars, some stars show clear emission line reversals even though $EW(H_\alpha) < 3 \text{ \AA}$ (Dahm 2008; Currie & Kenyon 2009). Devising a reliable metric for identifying accreting AFG stars is beyond the scope of this paper, so for AFG stars we nominally adopt the same $EW(H_\alpha)$ threshold applicable for K0–K7 stars and simply flag the few others showing core line reversal and H_α clearly in emission (no matter what the equivalent width).

Table 4 lists the 42 new candidate accreting stars and 30 previously-identified candidate accretors from Currie et al. (2007c). Of these 72 objects, 47 (51) are among our members with Spitzer (optical) photometry. Three were initially rejected in Currie et al. (2010) as likely members.

Despite the preferential sampling in favor of BAF stars, most of the new candidate accretors are G0 or later (38/42). Of the BAF stars listed in Table 4, two have H_α in absorption and thus formally are not identified as accretors. However, they have a strong core emission line reversal. These include a B9 star, which may be the earliest known accreting star older than 10 Myr. While the H_α equivalent widths generally are far smaller than for 1–5 Myr-old T Tauri stars and thus more indica-

tive of low accretion rates (White and Basri 2003; Dahm 2008), three early K stars have much stronger emission ($EW(H_\alpha) = 25\text{--}83 \text{ \AA}$) reminiscent of their younger counterparts. As our spectroscopic sample is very incomplete for the h and χ Persei mid K to M star population (Currie et al. 2010), it is unclear whether any of the kinds of stars comprising most members of the youngest star-forming regions show frequent H_α emission indicative of accretion in the Double Cluster.

4.2. Frequency of Accreting h and χ Persei Stars

Figure 11 shows that the accretion frequency for likely h and χ Persei members with optical spectra is highest for GK stars ($M \sim 0.8\text{--}1.3 M_\odot$) and lowest for earlier stars ($M > 1.4 M_\odot$). Our sample of accretors includes two F-type stars, while all the remaining accretors are G0 or later. As a result, the accretion frequency is consistent with zero from the earliest stars through F5, while the frequency rises above 2% for G0–K5 stars, peaking at $\sim 3.3\%$ for late G stars. This trend is consistent with a stellar mass dependent frequency of gas accretion (Currie & Kenyon 2009), although our criteria for identifying accretors may slightly underestimate this population around the earliest (BA) stars. The frequency is lower for K5–M0 stars, although here again our sampling is poor.

4.3. Accretion and Circumstellar Dust Emission

Recent results imply that the frequency of dust and gas in protoplanetary disks in most young clusters decreases on a timescale of ~ 3 Myr (Hernandez et al. 2007a; Currie & Kenyon 2009; Fedele et al. 2010; Currie and Sicilia-Aguilar 2011). However, the presence of dust in older, $\sim 10\text{--}20$ Myr old clusters does not necessarily imply detectable protoplanetary disk gas and vice versa. Many disks around 10–20 Myr old stars with dust emission are instead optically-thin, gas-poor debris disks (Chen et al. 2005; Roberge et al. 2008; Lisse et al. 2008, 2009). Conversely, at least some disks showing evidence for protoplanetary disk gas lack strong broadband infrared excess emission from dust that would be detectable in our sample (Currie et al. 2007c; Bitner et al. 2010). While preliminary results showed a weak correlation between protoplanetary disk gas and IR excess in h and χ Persei stars, our expanded sample of accretors and more precise IR photometry allows us to reinvestigate this connection.

Figure 11 compares the H_α equivalent width to the $[3.6]\text{--}[8]$ color amongst our sample of candidate accretors. Most strikingly, the distribution of IR colors appears nearly symmetrical about zero for a range of $EW(H_\alpha)$ with only 1–2 outliers. This result is in slight contrast with previous studies of h and χ Persei’s accreting population (Currie et al. 2007c), which found a very weak correlation between H_α equivalent width and $8 \mu\text{m}$ excess. Specifically, Currie et al. (2007c) derive a Spearman rank correlation coefficient of $r_s = 0.60$ across their full dynamic range in H_α equivalent width ($|EW(H_\alpha)| = 0\text{--}50 \text{ \AA}$). Conversely, over the same dynamic range, we derive a Spearman rank correlation coefficient of $r_s = 0.046$ implying that the relationship between protoplanetary disk gas and IR excess cannot be described by a monotonic function. The disagreement probably is due to 1) poorer

photometric precision in the Currie et al. (2007a) IRAC data and 2) the decision in Currie et al. (2007c) to use $K_s\text{--}[8]$ instead of $[3.6]\text{--}[8]$ as a tracer of warm dust, where the former exhibits a much stronger spectral type dependence (cf. Luhman et al. 2010).

5. SPECTRAL ENERGY DISTRIBUTION MODELING OF DISK-BEARING STARS

Analysis in §3 as well as previous work from Currie et al. (2007a, 2008a) demonstrates that h and χ Persei includes a small population of stars with 1) warm, terrestrial zone dust identifiable from broadband $8 \mu\text{m}$ excess emission and 2) very strong ($\gtrsim 3$ magnitude) excess emission at $24 \mu\text{m}$ that in many cases is likely due to cooler dust. As our observations are not sensitive to (pre-)main sequence stars lacking broadband $8 \mu\text{m}$ excess but producing modest $24 \mu\text{m}$ excesses ($\sim 0.25\text{--}1.5$ magnitudes) more typical around stars of comparable age (Chen et al. 2011), they cannot identify cooler debris disks and many homologously depleted transitional disks. Typical cold debris disks yield negligible broadband excesses at $24 \mu\text{m}$ and will also not be detected around h and χ Persei stars. While our study does not probe the full extent of the disk population, we still can analyze data for stars with IRAC and MIPS excesses or those that are accreting and compare the emission to that predicted for disks covering a range of evolutionary states. The disks around such stars represent those that are least evolved and provide an upper limit to the relative frequency of normal protoplanetary disks at 14 Myr .

5.1. Disk Terminology and Classification Method

Following Currie and Sicilia-Aguilar (2011), we consider three different classes of disks:

- **Primordial Disks** – We identify optically-thick primordial disks, characteristic of disks in the youngest star-forming regions (Gutermuth et al. 2009), generally as those with excess emission above our model disk limit from $4.5 \mu\text{m}$ to $24 \mu\text{m}$.
- **Transitional Disks with Inner Holes/Gaps** – We identify transitional disks with inner holes as those with photospheric emission or weak excess emission through $5.8 \mu\text{m}$ but emission in excess of our fiducial model at $24 \mu\text{m}$, indicative of a positive λF_λ slope from 8 to $24 \mu\text{m}$ and optically-thick outer disk emission at $24 \mu\text{m}$. Those with gaps like LkCa 15’s may appear to have emission comparable to an optically-thick disk at some near-IR wavelengths but have a steep flux slope ($\alpha \approx -3$) from the near to mid IR (e.g. through $8 \mu\text{m}$) due to an absence of dust between a hot optically-thick population near the dust sublimation radius and a cooler optically-thick population at AU -scale distances.
- **Warm Debris Disks/Homologously Depleted Transitional Disks** – Objects with weak excess, consistently lying below our fiducial disk model have SEDs comparable to homologously depleted transitional disks in Taurus, the Coronet Cluster, IC 348 and other young star-forming regions (Currie and Sicilia-Aguilar 2011) and warm debris disks (Currie et al. 2007b; Rhee et al. 2007;

Currie et al. 2008b). For all stars modeled here with spectra, none are shown to be accreting and thus none have clear evidence for circumstellar gas. However, our optical spectra were obtained at low resolutions, where weakly accreting disks may not be identifiable and/or may be difficult to flag. Although h and χ Persei's age may favor objects in this category as having warm debris disks (Currie et al. 2007b, 2008a), the case is not clear-cut. Thus, to be conservative we note that these objects may be *either* warm debris disk-bearing stars or those surrounded by homologously depleted transitional disks.

Note that our identification of candidate homologously depleted transitional disks is simpler than in Currie and Sicilia-Aguilar (2011) who focus on nearby clusters with richer IR data sets. Specifically, they used Taurus optical to submm data to identify the range of disk masses covered by optically thick primordial disks. In addition to the criteria listed above, they then required homologously depleted disks to have disk masses below the Taurus optically thick disk range. Some range in IR colors (e.g. $K_s - [8]$ vs. $K_s - [24]$) includes both primordial disks and transitional disks, but for clusters much more distant than Taurus (e.g. NGC 2362, h and χ Persei), we lack far-IR/submm data that is required to estimate a disk mass. Therefore, based on the Taurus modeling results, they correct for the frequency of transitional disks derived from IR SED modeling alone (as in this paper) by the 'contamination rate' of primordial disks with the same infrared excess emission. We do not introduce such a correction factor here since a) it is small to begin with and does not alter our results presented later and b) very few stars we model have IR colors that, based on Taurus data, correspond to multiple disk states.

5.2. Models Used to Classify Disks

5.2.1. Fiducial Disk Model Comparisons

We first compare the SEDs of disk-bearing h and χ Persei stars to geometrically flat, optically thick reprocessing disk models to conservatively identify those disks with a reduced optical depth of emitting dust ($\tau_{IR} \lesssim 1$): i.e. transitional disks. Following Currie and Sicilia-Aguilar (2011), we adopt models produced from the Whitney-Monto Carlo radiative transfer code (Whitney et al. 2003a,b; Robitaille et al. 2006). The models assume no flaring ($H/r = \text{constant}$), no accretion, and no protostellar envelope emission. The disks are optically thick to their own radiation over spatial scales relevant to our study ($r < 5\text{--}10$ AU) even for disks over an order of magnitude lower mass than that which we nominally adopt ($0.05 M_\odot$).

As shown in Currie and Sicilia-Aguilar (2011) and in other earlier publications (e.g. D'Alessio et al. 2006; Kenyon and Hartmann 1987), making the disk flared instead of flat or considering accretion can only result in a more luminous disk¹⁰ and a higher transitional disk fre-

quency. Therefore, our fiducial model represents a conservative limit separating the bluest, lowest-luminosity primordial disks from transitional disks.

5.2.2. Model SED Fitting

As a separate investigation, we model source SEDs using the grid of radiative transfer disk models from Robitaille et al. (2006). As our data are limited to detections at $\lambda \leq 24 \mu\text{m}$, these model comparisons cannot investigate the mass of emitting dust in the disks (Currie and Sicilia-Aguilar 2011), and our disk classification scheme does not turn on whether or not the disk is flared. Instead, we simply use these model comparisons to investigate whether each source's best-fit models require an inner hole substantially larger than the dust sublimation radius. Thus, they can show whether some disks we find lack inner holes (primordial disks, homologously depleted transitional disks) based on fiducial comparisons nevertheless are best-fit by a disk models with inner holes.

To identify the best-fitting disk models, we restrict ourselves to those models satisfying the $\Delta\chi^2$ criterion of $\chi^2 - \chi_{best}^2 < 3$, where χ^2 refers to the minimum χ^2 per data point (see also Currie and Sicilia-Aguilar 2011; Currie et al. 2009; Ercolano et al. 2009). We adopt a reddening uncertainty of 10% and a distance uncertainty of 10 pc. To be conservative, we set the division between a disk requiring an inner hole and one without at 10 times the dust sublimation radius.

5.3. Results for Disks with Excesses in Multiple Bandpasses

From our sample of ≈ 270 stars with infrared excess, 18 show clear excess at both $8 \mu\text{m}$ and $24 \mu\text{m}$ ¹¹, are later than B5 (fainter than $J = 13$) and thus not likely post-main sequence stars which can therefore be compared in more detail to disk models. One of these – $\alpha = 34.7824$, $\delta = 57.2346$ – was previously identified in Currie et al. (2007b, 2008a), labeled as "Source 5" since it was the fifth candidate h and χ Persei member with excesses in multiple IRAC bands, and modeled by comparing its SED to predictions from terrestrial planet formation calculations (Kenyon and Bromley 2004) and a simple model assuming two, single-temperature blackbodies. The other seventeen targets listed are new detections.

Of the 18 sources, 7 have optical spectroscopy from Currie et al. (2010). The remaining 11 lack optical spectroscopy and thus do not have a confirmed spectral type or extinction estimates. To determine the appropriate T_{eff} for these 11/18 stars, we first fit the V and I photometry to predicted colors for h and χ Per stars for a range of extinctions using intrinsic dwarf colors and reddening laws listed in Currie et al. (2010). The seven other targets had previously-derived spectral types and extinctions from Currie et al. (2010). We used these spectral types and extinctions as a starting point and explored whether alternative estimates provided a better fit to the optical/near-IR photometry. Our derived values agree with these previous determinations to within one

¹⁰ Inclination likewise has a negligible effect except for nearly edge-on cases (Currie and Sicilia-Aguilar 2011).

¹¹ Note again that this mismatch in numbers is largely driven by our poor sensitivity at MIPS-24 μm

subclass in spectral type and $\sim 10\%$ in reddening, supporting the parameters derived in Currie et al. (2010).

5.3.1. Results for Fiducial Disk Model Comparisons

Table 5 records the known or derived spectral types and reddening values along with IRAC/MIPS colors, and disk types of the 18 h and χ Persei stars with IRAC and MIPS excesses that we model. Figure 12 displays a typical model comparison with the model spectral type for the photosphere (Bb) and the disk (Disk) directly plotted along with its J2000 coordinates. We display an atlas of all modeled sources in the Appendix.

The majority (10/18) of these h and χ Per sources have SEDs most consistent with warm debris disks and/or homologously depleted transitional disks. Of the remaining sources, 6/18 have SEDs most characteristic of transitional disks with inner holes and only two objects have SEDs most consistent with primordial disks. Depending on whether we classify weak-excess sources as warm debris disks or homologously depleted disks, the relative fraction of protoplanetary disks in a transitional state is either 6/8 or 16/18. In either case, transitional disks outnumber the primordial disk population.

5.3.2. Results for SED Model Fitting

Table 5 (second column from the right) records the best-fit disk inner radius for our sources using the Robitaille et al. grid. Figure 13 displays example analysis results: the set of best-fit SEDs (left panel) and distribution of disk inner radii (right panel) for the eighth excess source in our list ($\alpha = 34.9447$, $\delta = 57.1925$). In most cases, our results based on fiducial model comparisons and model fitting agree. Primordial disks and homologously depleted transitional disks identified from fiducial model transitional disks, are not best-fit by a disk model with an inner hole. Disks with weak IRAC excess but much stronger MIPS-24 μm excesses are best-fit by disk models with large ($R_{\text{disk}} > 10 R_{\text{sub}}$) inner holes.

SED modeling suggests that we may be slightly underestimating the population of transitional disks with inner holes. Three sources, identified as having homologously depleted transitional disks/warm debris disks, are best fit by a disk model with an $R_{\text{disk}} > 10 R_{\text{sub}}$ hole. Two of these sources are early-type (B8.5, A5) stars with very weak, debris disk-like excess emission (0.2–0.6 mags in the IRAC bands; 1.6–1.75 mags in MIPS): the inner holes identified by SED modeling may instead reflect the location of debris belts. The third of these (F5.9) has a 4.7 magnitude excess in MIPS-24 μm characteristic of only the most luminous debris disks (e.g. HR 4796A Chen et al. 2005) and many transitional disks with inner holes (cf. Currie and Sicilia-Aguilar 2011). One source identified as having a primordial disk from fiducial model comparisons is best-fit by a disk model with a $30 R_{\text{sub}}$ inner hole.

In summary, our h and χ Persei disk analysis shows evidence for substantial evolution, even amongst the protoplanetary disk population. Fiducial model comparisons and SED fitting reveal a large fraction of transitional disks, either those with inner holes or ones that are homologously depleted, compared to primordial disks.

5.4. Results for Accreting Disks

In addition to our modeling of members with IRAC and MIPS excesses, we also briefly compare the SEDs of accreting members identified in §4 to the same fiducial disk model. While accreting circumstellar disks are often associated with optically-thick “primordial” disks that are typical of the youngest star-forming regions, Figure 14 shows that the situation is more complicated. The star with weaker H_α emission ($|\text{EW}(H_\alpha)| = 5.3 \text{ \AA}$ left panel) clearly has weaker warm dust emission relative to the optically-thick, geometrically flat disk limit. The other star, the outlier in Figure 11 (right panel), has significantly stronger H_α emission ($|\text{EW}(H_\alpha)| = 47.32 \text{ \AA}$) but still has IRAC excess emission from dust lying at or below the flat disk limit (Figure 14, right panel). The SEDs of the remaining accreting stars that also maintain an IRAC excess, resemble the left-hand panel star, as the strength of the excess is always weaker than the flat, optically-thick disk limit.

Therefore even the long-lived accreting protoplanetary disks in h and χ Persei show evidence for significantly reduced broadband IR dust emission more indicative of transitional disks than the optically thick *primordial* disks that dominate the youngest star-forming regions like Taurus. In the next section, we compare the frequency and morphologies of disks in h and χ Persei to those in other clusters in a global analysis of disk evolution from 1 Myr to 20 Myr.

6. THE h AND χ PERSEI DISK POPULATION IN CONTEXT: EMPIRICAL CONSTRAINTS ON DISK EVOLUTION AND PLANET FORMATION

6.1. Methodology and Goals

Comparing the disk population in h and χ Persei to that for clusters/associations of comparable or younger ages allows us to constrain how the frequency of warm circumstellar dust and gas changes with time (Hernandez et al. 2007a; Fedele et al. 2010; Currie and Sicilia-Aguilar 2011, see). Circumstellar dust and gas comprise the building blocks of planetary cores and gaseous envelopes (Pollack et al. 1996; Kenyon and Bromley 2009); dust may also be second-generation, produced via collisions between planetesimals in young debris disks (Wyatt 2008; Kenyon and Bromley 2008). Modeling the time evolution of dust and gas then sets some limits on the timescale for converting these raw materials into gas giant planets and/or the early time evolution of debris disks (Rieke et al. 2005; Su et al. 2006; Currie et al. 2008a, 2009; Chen et al. 2011, 2012).

In this section, we combine h and χ Persei data with that from other clusters to explore the timescale for protoplanetary disk evolution and the properties of debris disks, especially those around high-mass stars ($4\text{--}6 M_\odot$). Although we use specific, absolute (and hence uncertain) ages to describe the clusters, our arguments are chiefly based on the *relative* ages and the evolutionary sequence they establish, which Soderblom et al. (2014) argue are robust. Table 6 lists the clusters/associations we consider and their frequencies of circumstellar dust and gas. The samples probe well into the M dwarf, subsolar-mass regime. Due to the extreme sample size of h and χ Persei stars we achieve robust estimates of the warm dust and gas fractions at $\sim 10\text{--}15 \text{ Myr}$.

First, we follow Currie and Sicilia-Aguilar (2011), us-

ing a Monte Carlo simulation to predict the frequency of circumstellar gas and dust from protoplanetary disks for various characteristic dust/gas evolution e-folding timescales. We then identify the timescale that best matches the data using a simple reduced χ^2 criterion. We use the best-fitting dust evolution timescale as input for a second Monte Carlo simulation tracing the relative frequency of transitional disks with time for various bulk transition disk timescales ranging between 0.1 *Myr* and 1 *Myr* using the subset of well-characterized clusters in Currie and Sicilia-Aguilar (2011) – Taurus, the Coronet Cluster, IC 348, NGC 2362, η Cha – and h and χ Persei. Finally we explore debris disk evolution for stars with masses $\sim 4\text{--}6 M_{\odot}$, a mass range not previously studied, by comparing the frequency of MIPS-excess sources in h and χ Persei to those for members of the Sco-Cen Association (Upper Scorpius, Lower Centaurus Crux, and Upper Centaurus Lupus) (Chen et al. 2011, 2012). All data probing dust evolution come from *Spitzer* observations, whereas data probing gas evolution originate from various ground-based spectroscopic surveys.

While our data probing circumstellar dust draw from *Spitzer*/IRAC observations only, some differences between each cluster sample impede our ability to set more robust limits on the typical timescale for protoplanetary disks to disappear. For instance, the completeness limits for each cluster data set are different. This is especially true for h and χ Persei, which is more distant than the other clusters analyzed here. Although our methods for identifying excess sources follow those standard in the literature (Hernandez et al. 2007a), there may still be small differences between methods used to find disk-bearing stars amongst the clusters we analyze.

With these caveats in mind, we focus simply on understanding the typical evolution timescales for warm dust and gas and how these timescales change depending on the assumed ages for clusters. For example, recent work by Peca et al. (2012) argues that Upper Scorpius may be about twice as old as its nominal 5 *Myr* age (Preibisch et al. 2002), although other work seems to indicate results intermediate between these extremes (Bowler et al. 2011). Bell et al. (2013) reinvestigate the ages of many young clusters – e.g. IC 348, σ Orionis, and NGC 2362 – often used to define these evolutionary timescales and argue that cluster ages have generally been underestimated. However, Bell et al. (2013) find an age for χ Persei (14.5 *Myr*) in excellent agreement with previous estimates (14 *Myr*, Currie et al. 2010).

To bracket the error range for young cluster ages (Soderblom et al. 2014), we fit for the warm dust and gas evolutionary timescales assuming nominal cluster ages and those revised in Bell et al. (2013) and Peca et al. (2012), while keeping the age of h and χ Persei fixed at 14 *Myr*. We then use the best-fit timescales as input to investigate the transitional disk lifetime as in Currie and Sicilia-Aguilar (2011), including our new results for h and χ Persei.

6.2. Evolution of Warm Dust from Inner Disks

Figure 15 plots the frequency of warm dust emission (as probed by *Spitzer*/IRAC) for our sample, where we focus on clusters with ages between 1 and 15 *Myr*. The best-fit timescale is 2.75 *Myr*. We obtain similar results regardless of whether we focus on all clusters or

just those nominally younger than 10 *Myr*. While this timescale best reproduces our combined sample there are clearly outliers, most notably Trumpler 37 and the very sparse association η Cha (Sicilia-Aguilar et al. 2006; Megeath et al. 2005; Sicilia-Aguilar et al. 2009). The frequencies for Taurus and NGC 7129 also appear somewhat low, though in Taurus’s case binarity may play a role in affecting disk frequencies (cf. Kraus and Ireland 2012). In both cases, h and χ Persei lies slightly above the trendline we expect for warm dust originating only from protoplanetary disks.

The middle panel displays a model with a slightly longer timescale ($t(\text{PD}) = 3.25$ *Myr*), which together with 2.75 *Myr* bracket the value considered by Currie and Sicilia-Aguilar (2011). The near-quadrupling of the reduced χ^2 as the model timescale increases to 3.25 *Myr* is largely due to the inability of the model to reproduce the dust frequencies found in regions such as σ Orionis (Hernandez et al. 2007a), Upper Scorpius (Carpenter et al. 2006), and NGC 2362 (Dahm and Hillenbrand 2007; Currie et al. 2009).

Adopting revised ages for clusters listed in Bell et al. (2013) and Peca et al. (2012) clearly yields a longer timescale (right panel) for warm dust in disks. Our best-fit timescale ($\chi^2_{\nu} \sim 2.4$) more than doubles to 5.75 *Myr*, a result driven by some of the same regions (σ Orionis, Upper Scorpius, and NGC 2362) whose frequencies determine the best-fit timescale for nominal ages. When assuming the revised cluster ages of Bell et al. (2013), the 2.75 *Myr* timescale found to best fit the combined sample when nominal ages are adopted clearly underpredicts the disk frequencies for IC 348, σ Ori, Upper Sco, and NGC 2362 ($\chi^2_{\nu} \sim 22$). For h and χ Persei however, an intermediate timescale may be more consistent.

6.3. Evolution of Protoplanetary Disk Gas

Our results for circumstellar gas evolution mimic the general trends found in the above section for dust (Figure 16). The best-fit accretion timescale adopting nominal cluster ages is 1.75 *Myr* ($\chi^2_{\nu} \sim 1.4$), slightly smaller than our nominal dust timescale and marginally consistent with previous analyses (Fedele et al. 2010). The predicted gas disk frequency as a function of time well matches the combined sample with the possible exception of ρ Oph where it overpredicts the accretion frequency and slightly older ($t > 5$ *Myr*) regions like η Cha and 25 Ori, where it underpredicts the accretion frequency.

As with dust, the revised cluster ages for many clusters significantly extend the gas disk lifetime. Our best-fit value is $\tau_o = 3.75$ *Myr*, more than a factor of two longer than the timescale we obtain from nominal cluster ages. Taken literally, adopting revised cluster ages yields gas disk timescales slightly shorter than warm dust lifetimes, in slight contrast to previous results finding similar lifetimes for gas and dust (Fedele et al. 2010; Currie & Kenyon 2009). Although sample-specific biases in how disk dust and gas may instead be responsible for these differing gas and dust lifetimes, the more basic result is robust: the revised cluster ages would more than double the gas and warm dust lifetimes.

6.4. Transitional Disk Evolution

Figure 17 compares transitional disk frequencies derived for Taurus, the Coronet Cluster, IC 348, NGC 2362, and η Cha from Currie and Sicilia-Aguilar (2011) with those derived here for our limited h and χ Persei sample. Lines denote predicted transitional disk frequencies from our Monte Carlo simulations for a range of bulk transitional disk durations ranging between 0.1 *Myr* and 2 *Myr* assuming a protoplanetary disk lifetime of 2.5 *Myr* for nominal cluster ages (left) and 6 *Myr* for revised ages (right). For h and χ Persei, the error bars correspond to upper and lower limits for the transitional disk frequency determined from whether stars with weak excesses are considered to be homologously depleted transitional disks or warm debris disks. For other clusters, the error bars likewise reflect ambiguities in interpreting the properties of the most weakly-emitting disks (see discussion in Currie and Sicilia-Aguilar 2011).

Despite uncertainties in inferring the properties of many disks, our analysis clearly points to a transitional disk phase that lasts ≈ 1 *Myr* when averaged over entire cluster samples and all possible pathways: transitional disks with holes/gaps depleted in dust that clear from the inside-out and those that deplete homologously. For revised ages for IC 348, NGC 2362 and other clusters, this trend is even stronger. For all cases, the transitional disk phase lasts on average $\approx 1/4$ – $1/3$ of the total protoplanetary disk lifetime. Our results are consistent with recent detailed studies of transitional disk frequencies (Currie and Sicilia-Aguilar 2011; Currie et al. 2009).

Many sources in the oldest clusters – i.e. NGC 2362, h and χ Per – identified as having homologously depleted transitional disks may instead have warm debris disks. Nevertheless, considering primordial disks and transitional disks with inner holes alone for these clusters still point to an extended transitional disk duration. For NGC 2362 and h and χ Persei, we would still derive transitional disk fractions of 5/9 and 6/8, respectively (cf. Currie & Sicilia-Aguilar 2011 for NGC 2362; this work for h and χ Per), which are consistent with a 1 *Myr*-long average transitional disk phase.

6.5. Frequency of Dust around 4–6 M_{\odot} stars

Although the relatively shallower depth of MIPS compared to IRAC for stellar photospheres means we have far weaker constraints on the presence of cooler dust producing 24 μm excess emission, the MIPS data are deep enough that we can compare frequencies for massive stars to those for similar stars in other clusters. Figure 18 compares the frequency of dust around 4–6 M_{\odot} stars to those for the Sco-Cen subgroups: Upper Scorpius (5–10 *Myr*), Upper Centaurus Lupus (16 *Myr*) and Lower Centaurus Crux (17 *Myr*). To derive frequencies for Sco-Cen we focus on B2–B6 stars and simply compare the number flagged as excess sources in Carpenter et al. (2009b) and Chen et al. (2012), trimming out Be stars and post-main sequence objects.

All samples exhibit a very low frequency of 24 μm excess from disks around 4–6 M_{\odot} stars, ranging between zero and $\sim 7\%$ (0/4 for Upper Sco, 0/8 for LCC, and 1/14 for UCL). The small sample sizes and small numbers of excess sources preclude us from identifying any trend in 24 μm excess frequency vs. time as has been found for 1.5 M_{\odot} stars (Currie et al. 2008b). However, these massive stars exhibit lower MIPS-24 μm excess frequencies

than do 1–2.5 M_{\odot} stars at 10–30 *Myr* for many clusters (~ 25 – 50% Currie et al. 2008b; Forbrich et al. 2008; Chen et al. 2011, 2012).

7. DISCUSSION

7.1. Summary of Results

We present new constraints on the time evolution of planet forming disks from new, deep IRAC and MIPS photometry of $\sim 12,500$ stellar members of the Double Cluster, h and χ Persei, deeper at 8 μm and 24 μm by ~ 1.5 magnitudes compared to previous studies (Currie et al. 2007a, 2008a). Relative to regions of a similar age, the Double Cluster contains a large sample of stars which is vital for producing robust statistical estimates of the frequency of warm dust and gas.

Our study yields the following primary results:

- The frequency of warm dust, as probed by IRAC 8 μm excess, is on the order of ~ 2 – 3% for the sample as a whole, increasing from near zero for mid-B stars to ≈ 4 – 5% for sub-solar mass stars.
- Although the MIPS 24 μm data are not sufficiently deep to conduct a similar analysis for all h and χ Persei members, they provide the first constraints on the disk frequency for the region’s most massive planet-bearing stars (4–6 M_{\odot}). About ~ 3 – 8% of these massive stars have MIPS-24 μm excesses, lower than the MIPS-24 μm frequencies found for 1–2.5 M_{\odot} stars in other clusters.
- The frequency of accretion amongst h and χ Persei stars is $\sim 2\%$, comparable to the warm dust frequency. Similarly, the accretion frequency may be higher for later type, lower-mass stars. We do not find evidence for a correlation between the presence of warm dust and accreting gas.
- SED modeling of h and χ Persei stars with IRAC and MIPS excesses allows us to investigate the morphology of rare disks with warm dust at 10–15 *Myr*. Our modeled stars have disks exhibiting a wide range of evolutionary states. In particular, a large fraction of disks appear to have SEDs consistent with transitional disks, indicative of a rather extended transitional disk duration.
- We combine our results for h and χ Persei to those for other clusters to conduct a global analysis of disk evolution in young clusters. Assuming nominal cluster ages, we derive characteristic e-folding timescales of 2.75, 1.75, and 1 *Myr* for the warm dust lifetime, gas lifetime, and transitional disk duration. Assuming alternate cluster ages (Bell et al. 2013; Pecaute et al. 2012), these timescales increase to 5.75, 3.75, and 1.5 *Myr*, respectively. Thus, the protoplanetary disk phase may last significantly longer than previously thought.

7.2. Comparisons with Earlier Studies

7.2.1. Earlier Studies of the Disk Population of h and χ Persei

This study builds upon analyses of Cycle 1 IRAC and MIPS Spitzer and ground-based data, which comprised the first studies of circumstellar disks around stars in the Double Cluster (Currie et al. 2007a,b,c, 2008a). Over an area comparable to this study, Currie et al. (2007a) identified about 5000 (7000) stars detected in the IRAC [8] ([4.5]) filters and located near previously known members of h and χ Per, used 2MASS all-sky survey data to select stars whose near-IR color-magnitude diagram positions were plausibly consistent with those for 2.3 kpc distant stars, and studied the frequency of warm IRAC excess emission by comparing photometry derived from 2MASS K_s to IRAC flux densities. Currie et al. (2007b) identified a subsample of stars with IRAC excesses in multiple bands, added in preliminary MIPS photometry, and compared the stars' SEDs to model predictions for warm debris disks whose dust is indicative of active terrestrial planet formation. Currie et al. (2007c) identified about two dozen stars whose color-magnitude diagram positions were consistent with values expected for h and χ Persei members and whose H_α equivalent widths were consistent with estimates for accreting objects. Finally, Currie et al. (2008a) present a full analysis of MIPS data for h and χ Persei, modeled systems with strong MIPS-excess emission, and compared MIPS 24 μm excesses around BAF stars from multiple regions to investigate the time evolution of 24 μm debris emission.

The data analyzed in our study differ from previous data in several important respects. Our IRAC data are significantly deeper, with completion limits roughly two magnitudes deeper in [8]; at the completion limits for the Cycle 1 data, our photometric errors are ≈ 3 times smaller. We achieve similar increases in survey depth at MIPS 24 μm . While Currie et al. (2007c) draw from preliminary analysis of 5000 stars with optical spectroscopy, our study incorporates the full sample. These previous studies either focused on all 2MASS-detected objects in the field or relied on very preliminary photometric cuts to focus on candidate members. Our study uses the candidate membership list from Currie et al. (2010) based on extremely deep optical photometry and optical spectroscopy to remove background stars from our analysis.

Our results modify some previous conclusions about h and χ Persei's disk population. Currie et al. (2007a) found that few ($\sim 2-3\%$) stars have excesses at multiple IRAC bands, although the frequency of such excesses rose towards fainter stars likely representative of later, lower-mass stars. We derive similar frequencies at 8 μm near our survey depth limit. For brighter stars probed by Currie et al. (2007a), our frequencies are lower likely because our criterion for differentiating between an IR excess source and a bare stellar photosphere is more conservative and based on the observed dispersion of IRAC colors as a function of magnitude. While our accretor frequency agrees with rough estimates previously reported by Currie et al. (2007c), we fail to confirm the trend between IRAC excess and H_α equivalent width indicated by their preliminary analysis.

Currie et al. (2007b) and Currie et al. (2008a) identify stars with weak IRAC excesses as candidate terrestrial planet-forming systems. A full analysis of the optical

spectroscopy sample and the IRAC data together demonstrates that h and χ Persei contains a mixed disk population: sources with evidence for gas but no dust, dust but no evidence for gas, and those with evidence for both. It is likely that many (most?) of our weak IRAC excess sources are terrestrial planet forming systems, since such systems are found around more nearby, better studied stars (Rhee et al. 2007; Lisse et al. 2008). However, to be conservative we remain agnostic as to the state of these systems: they could either be warm debris disks or homologously depleted transitional disks.

Finally, we did not reinvestigate the “rise and fall” of 24 μm emission from debris disks around BAF stars. Although a full analysis of these targets within the context of debris disk evolution will be left for a future paper, studies published subsequent to Currie et al. (2008a) support a more limited version of our previous results. For example, Carpenter et al. (2009a) find evidence for a peak in debris emission around F stars at $\sim 10-15 Myr$ but do not find a similar trend for earlier or later-type stars. Focusing only on planet mass (by accounting for the different mapping between spectral type and mass vs. age), Chen et al. (2011) find evidence for an increase in debris emission at 15–20 Myr (the age of the older Sco-Cen subgroups) around 1.5 M_\odot stars. But this behavior is not seen so clearly for solar-mass stars nor for 2–2.5 M_\odot stars. While Currie et al. (2008a) and later Kenyon and Bromley (2008) interpret a peak in debris emission within the context of oligarchic growth in icy planetesimal swarms, Chen et al. (2011) argue that the debris luminosities for solar-mass stars are *higher* than predicted in debris disk evolution models. The distribution of debris disk temperatures as a function of stellar mass and age also may hint at key effects not explicitly considered in the Kenyon and Bromley models such as planetesimal belt sculpting by massive planets (e.g. Chen et al. 2014).

7.2.2. The Lifetime of Protoplanetary Disks and Timescale for Gas Giant Planet Formation

This work provides a quantitative, updated comparison to earlier estimates of the lifetime of warm dust and gas in protoplanetary disks and assessment of how stellar age uncertainties affect derived lifetimes. From ground-based L' data of many clusters, Haisch et al. (2001) compare disk frequencies to a simple linear fit and estimate that half of all protoplanetary disks disappear by $\sim 3 Myr$ and nearly all disappear by 6 Myr . Based on deeper Spitzer/IRAC data able to detect the stellar photosphere of subsolar mass stars and at wavelengths where disk excess is more easily identifiable (see discussion in Ercolano et al. 2009), Hernandez et al. (2007a) estimate a typical lifetime of $\approx 3 Myr$ as well. Fedele et al. (2010) match frequencies of gas and dust to an exponential decay function; Currie and Sicilia-Aguilar (2011) match the dust frequency to Monte Carlo simulation predictions with an exponential decay probability distribution function as in this work. In all cases, the results are similar: a protoplanetary disk gas and dust lifetime of $\approx 2.5-3 Myr$ for most stars (see also Mamajek 2009; Jayawardhana et al. 2006), slightly shorter (longer) for early-type higher mass (mid M) stars (see Carpenter et al. 2006; Currie & Kenyon 2009).

Assuming nominal cluster ages, we derive fairly sim-

ilar results, although we, like Fedele et al. (2010), formally favor a slightly longer e-folding timescale for dust than gas ($\tau_{dust} \sim 2.75 \text{ Myr}$ and $\tau_{gas} \sim 1.75 \text{ Myr}$). This may be due to some mixing of disk populations: e.g. some of the warm dust may be from terrestrial zone debris emission, not protoplanetary disk dust, so that our protoplanetary disk frequency is overestimated. Alternatively, surveys may be failing to identify some stars whose weak optical emission lines and veiling from accretion are best identified from high signal-to-noise, high resolution echelle spectra (see Dahm 2008).

Our results support and quantify Bell et al. (2013)’s assertion that alternate ages derived for many young clusters would significantly lengthen the inferred lifetimes for protoplanetary disk dust. As expected, the gas disk lifetime is also longer. Bell et al. (2013) quote a “half-life” of disks of 5–6 *Myr* and report a 10–20% disk fraction at 10–12 *Myr*. Assuming that the disk lifetime decays as an exponential function and including slightly different samples (i.e. Upper Scorpius instead of the more distant λ Ori), our Monte Carlo analysis yields largely similar results for dust: $\tau_{dust} \sim 5.75 \text{ Myr}$ and a dust fraction of ≈ 10 –20% at 10–12 *Myr* and then $< 5\%$ at later ages. While the gas disk lifetime we derive is shorter ($\approx 3.75 \text{ Myr}$) it is still more than twice as long as the one we derive assuming nominal cluster ages.

At present, it is not yet clear which set of ages is correct (Soderblom et al. 2014), although older ages derived for pre-main sequence stars in Upper Scorpius are more consistent with ages derived for the region’s post-main sequence population (see Peca et al. 2012)¹². Thus, these different estimates should be understood to bracket possible values. While the stars we focus on are predominantly solar to slightly subsolar in mass, the disk lifetime may be even longer for the latest stars and highest-mass brown dwarfs: for $\approx 10 \text{ Myr}$ -old Upper Scorpius, Luhman and Mamajek (2012) still find that 1/4 of all mid M stars show evidence for warm circumstellar dust.

A revised, more lengthy characteristic protoplanetary disk lifetime would have important consequences for planet formation, especially for gas giants. For instance, wide separation super-jovian mass planets discovered through direct imaging (Marois et al. 2008) are extremely difficult to form via standard core accretion models (Pollack et al. 1996), yet at least some of them have properties (e.g. mass ratio/separation; C/O abundances) suggesting that they may have formed this way (Currie et al. 2011; Konopacky et al. 2013). Modifications to core accretion models (Lambrechts & Johansen 2012; Kenyon and Bromley 2009) are required to account for these cores within the nominal, short protoplanetary disk lifetime. With the exception of ROXs 42B (Currie et al. 2014), the host stars for these planet-mass companions are older than either the nominal or revised protoplanetary disk lifetimes. Thus, a longer disk lifetime relaxes these constraints placed on planet formation by core accretion as well.

7.2.3. Duration of the Transitional Disk Phase

¹² While every age derivation is model dependent, arguably the least model-dependent age-dating method (Li depletion) likewise favors systematically older ages for regions previously age-dated to 10 *Myr* (e.g. Binks and Jeffries 2014).

Our analyses support previous results (Currie et al. 2009; Currie and Sicilia-Aguilar 2011) finding that the transitional disk phase lasts longer than proposed in most early studies (Skrutskie et al. 1990; Wolk and Walter 1996), closer to 1 *Myr* than 0.1 *Myr*. In contrast, a few recent studies which use empirical breaks in IR colors alone arrive at somewhat shorter durations (Luhman et al. 2010; Luhman and Mamajek 2012). The major drawback with these other recent studies is that IR colors alone do not accurately distinguish between normal protoplanetary disks and disks that are becoming optically thin, since the color space between the two populations overlaps (Merin et al. 2010; Currie and Sicilia-Aguilar 2011)¹³. Thus, a criterion for identifying transitional disks based on perceived breaks in IR colors will underestimate this population’s size and in turn underestimate the transitional disk duration.

To alleviate these shortcomings, Currie and Sicilia-Aguilar (2011) adopt the SED modeling-driven criteria described in their §4.2 and briefly summarized in §5.2 in this work. While Luhman and Mamajek (2012) rightly note that theoretical models are imperfect and have degeneracies, Currie and Sicilia-Aguilar (2011) explicitly addressed these issues by treating their classifications probabilistically. For instance, the intrinsic distribution of their modeling grid in disk mass is heavily biased towards high masses. Their SED modeling identifies many transitional disks in spite of this strong prior in favor of classifying a disk as primordial¹⁴.

The key addition used in Currie and Sicilia-Aguilar (2011)’s classifications – a disk mass limit separating some transitional disks from primordial disks – is justified. Our ignorance of the dust opacity and assumed (not measured) dust-to-gas ratios for many disks precludes an absolute calibration of disk masses (Currie and Sicilia-Aguilar 2011). However, since disk masses for both primordial disks and (candidate) transitional disks were derived self-consistently, we can identify whether or not homologously depleted transitional disks have *relatively* lower masses. Although Currie and Sicilia-Aguilar (2011)’s adopted limit ($0.1\% \times M_*$) was typically just above the detec-

¹³ For example, many “gapped” transitional disks (e.g. LkCa 15, UX Tau, MWC 758) have “normal” IR colors but large, $\gtrsim 10 \text{ AU}$ -wide cavities indicative of disk clearing and likely opened by infant planets (Espanillat et al. 2010, 2012; Andrews et al. 2011; Dodson-Robinson and Salyk 2011). Since these disks have experienced significant structural evolution, they cannot be considered ‘primordial’ as claimed in Luhman and Mamajek (2012), since disks are not born with 50 *AU*-scale gaps in large dust. Homologously depleted transitional disks likewise overlap in some IR color space with normal protoplanetary disks.

¹⁴ Luhman and Mamajek (2012) also cite Espanillat et al. (2012) as highlighting ZZ Tau as a candidate transitional disk that could also be fit by a primordial disk model with significant dust settling. However, the Espanillat et al. model is optically thick only over tiny, $\sim \text{AU}$ scales, while the modeled disk size is $\approx 100 \text{ AU}$. Visual inspection of their Figure 13 indicates that their the model overpredicts emission at *K*-band and the IRAC bands, which comes from hot dust located at these inner disk regions. Our own model comparisons suggest that ZZ Tau has only a clear broadband excess at $\lambda \geq 4.5 \mu\text{m}$ (Currie and Sicilia-Aguilar 2011). Thus, their optical depth in inner disk regions is likely overestimated. Finally, they require a significantly lower disk mass than typically reported for optically thick disks ($5 \times 10^{-4} M_\odot$), which is precisely the point made in Currie and Sicilia-Aguilar (2011).

tion limit for most of the submm data we considered (Andrews and Williams 2005), nearly all of the optically-thick disks in Andrews and Williams (2005) were detected, and Currie and Sicilia-Aguilar (2011) modeled *all* of them anyway. Candidate homologously depleted disk masses can then be compared to the mass distribution for primordial disks.¹⁵

In summary, detailed modeling of very young nearby clusters like Taurus, coarser modeling of populous older regions like NGC 2362 and η and χ Persei, and statistical analyses of multiple clusters support a more lengthy transitional disk duration of ≈ 1 Myr. Averaged over entire clusters and over all possible disk clearing mechanisms, transitional disks occupy about 1/4 to 1/3 of the total disk lifetime. As shown in this paper, the upwards-revised ages for clusters in Bell et al. (2013) and Peca et al. (2012) only serve to strengthen the argument in favor of a more extended transitional disk duration.

7.3. Future Work

The Double Cluster, η and χ Persei, provides an excellent laboratory with which to study stellar evolution from the pre-main sequence to post-main sequence (Currie et al. 2010; Bell et al. 2013; Slesnick et al. 2002) and circumstellar disks at an age probing the protoplanetary to debris disk transition (this work; Currie et al. 2007a, 2008a). Currie et al. (2010) highlighted several key areas of future research on η and χ Per's stellar population, and here we list future avenues of research to study its disk population:

- **Disk Evolution as a Function of Environment** – As noted in Currie et al. (2010), the coverage area for optical spectra is substantially larger than that for the optical photometry we combine it with to establish a list of members, meaning that there could be many more stars associated with the halo population of η and χ Persei (Currie et al. 2007a) that we have yet to identify. A wide-field optical photometric survey would identify additional candidate members of η and χ Persei. Furthermore, because our Cycle 1 Spitzer data (and, to a lesser extent, the data we present here) were obtained over a similarly large area, we could compare the frequency of warm dust/gas between stars in the low density regions to those in the cluster-dominated regions to better understand how disk evolution depends on the circumstellar environment. Recent studies indicate that disk lifetimes may be significantly longer for extremely tenuous associations (Fang et al. 2013), or much shorter in extremely dense globular cluster-like environments (Thompson 2013). The Double Cluster allows us to study the environmental dependence of the fre-

quency of warm dust in disks within a single coeval region.

- **The Disk Properties of Subsolar-Mass Stars** – Our current spectroscopic sample does not well probe the η and χ Persei disk later than \sim mid G (see Fig. 6 in Currie et al. 2010). In addition to identifying low-mass (candidate) members, optical spectroscopy such as with MMT/Hectospec (and later Binospec) or LBT/MODS could measure accretion diagnostics (e.g. H_{α}) that will allow us to better characterize the properties of the faintest stars with IRAC and MIPS excesses. In principle, we could see whether all such stars show evidence for accretion or, like the stars studied here, include both stars showing evidence for gas (protoplanetary disks) and those lacking evidence for gas (candidate debris disk-hosting stars).
- **Observations of the η and χ Persei Disk Population with *JWST*** – Finally, the *James Webb Space Telescope* (*JWST*) should provide a significant advance in our understanding of the Double Cluster's disk population. In particular, while Spitzer/IRAC data are highly sensitive to photospheric emission/weak excesses around subsolar mass stars, our sensitivity further into the infrared is far poorer, as MIPS is only sensitive to the photospheres of early/mid B stars (see §2.5).

In contrast, MIRI with *JWST* has a $50\times$ smaller beam size and a predicted $5\text{-}\sigma$, 2500 s sensitivity of $28 \mu\text{Jy}$ at $25.5 \mu\text{m}$, or roughly two magnitudes fainter than our typical MIPS-24 μm limits, capable of detecting the photosphere of early A stars in the Double Cluster. Sensitivity gains at slightly shorter wavelengths (e.g. $20 \mu\text{m}$) are even more substantial, allowing us to study disks around even lower-mass stars. The far superior mid-IR sensitivity of *JWST*/MIRI then means we will better be able to put a study of η and χ Per's disk population on a more comparable footing to other less populous but much closer regions (e.g. Sco-Cen; σ and λ Orionis).

We thank the anonymous referee for suggestions that improved the quality of this paper. John Carpenter and Eric Mamajek also provided very helpful early draft comments and other suggestions that improved the quality of this paper. We also thank Andras Gaspar, Todd Thompson, and Cameron Bell for additional helpful conversations. T.C. is supported by a McLean Postdoctoral Fellowship.

¹⁵ Subsequent, deeper (sub)mm data do not change this result. Andrews et al. (2013) find that their sample, which includes both optically thick disks and those that are optically thin in the near-to-mid IR (e.g. V819 Tau, V410 X-ray 6, FP Tau, ZZ Tau, have submm-inferred masses of 0.2–0.6 %. The lower-quartile of their $M_{\text{disk}}/M_{\odot}$ distribution does extend below 0.1%, but the masses are estimated from the submm alone and this trend is most likely driven by submm non-detections. Similar trends in Andrews and Williams (2005) (“full sample” and their Table 2 sample) were not recovered by Currie and Sicilia-Aguilar (2011) who estimated disk masses from modeling *all* data, not estimating masses based solely on the submm flux. SED modeling-derived masses for the Andrews et al. (2013) will be higher and will further widen the gap between Currie and Sicilia-Aguilar (2011)'s adopted limit and the mass range for normal, primordial disks. Data for older clusters reinforce this point. Luhman and Mamajek (2012) argue based on K_s -[24] colors that Taurus and 10 Myr-old

REFERENCES

- Adams, F. C., Lada, C. J., & Shu, F. H. 1987, *ApJ*, 312, 788
- Aigrain, S., et al., 2007, *MNRAS*, 375, 29
- Andrews, S., Williams, J., 2005, *ApJ*, 631, 1134
- Andrews, S., et al., 2011, *ApJ*, 732, 42
- Andrews, S., et al., 2013, *ApJ*, 771, 129
- Baraffe, I., et al., 1998, *A&A*, 337, 403
- Bell, C. P. M., Naylor, T., Mayne, N. J., Jeffries, R. D., & Littlefair, S. P. 2013, *MNRAS*, 434, 806
- Binks, A., Jeffries, R. D., 2014, *MNRAS*, 438, 11
- Bitner, M., et al., 2010, *ApJ*, 714, 1542
- Bowler, B., et al., 2011, *ApJ*, 743, 148
- Bragg, A., Kenyon, S., 2002, *AJ*, 124, 3289
- Briceno, C., et al., 2007, *ApJ*, 661, 1119
- Calvet, N., et al., 2004, *AJ*, 128, 1294
- Calvet, N., D'Alessio, P., Watson, D. M., et al. 2005, *ApJ*, 630, L185
- Carpenter, J., et al., 2006, *ApJ*, 651, L49
- Carpenter, J., et al., 2009a, *ApJS*, 181, 197
- Carpenter, J., Mamajek, E., Hillenbrand, L., Meyer, M., 2009, *ApJ*, 705, 1646
- Chen, C., et al., 2005, *ApJ*, 602, 985
- Chen, C., et al., 2011, *ApJ*, 738, 122
- Chen, C., et al., 2012, *ApJ*, 756, 133
- Chen, C., et al., 2014, *ApJS*, 211, 25
- Currie, T., et al., 2007a, *ApJ*, 659, 599
- Currie, T., et al., 2007b, *ApJ*, 663, 105L
- Currie, T., et al., 2007c, *ApJ*, 669, 33L
- Currie, T., 2008, PhD Thesis, University of California-Los Angeles
- Currie, T., et al., 2008a, *ApJ*, 672, 558
- Currie, T., Plavchan, P., Kenyon, S. J., 2008b, *ApJ*, 688, 597
- Currie, T., & Kenyon, S. J. 2009, *AJ*, 138, 703
- Currie, T., Lada, C. J., et al., 2009, *ApJ*, 698, 1
- Currie, T., Hernandez, J., Irwin, J., et al., 2010, *ApJS*, 186, 111
- Currie, T., et al., 2011, *ApJ*, 729, 128
- Currie, T., Sicilia-Aguilar, A., 2011, *ApJ*, 734, 115
- Currie, T., et al., 2014, *ApJ*, 780, L30
- D'Alessio, P., et al., 2006, *ApJ*, 638, 314
- Dahm, S., Hillenbrand, L., 2007, *AJ*, 133, 2072
- Dahm, S., 2008, *AJ*, 136, 521
- Dent, W. R. F., Thi, W. F., Kamp, I., et al. 2013, *PASP*, 125, 477
- Dodson-Robinson, S., Salyk, C., 2011, *ApJ*, 738, 131
- Dullemond, C. P., & Dominik, C. 2005, *A&A*, 434, 971
- Ercolano, B., Clarke, C., Robitaille, T., 2009, *MNRAS*, 394, L141
- Españolat, C., Calvet, N., D'Alessio, P., et al. 2007, *ApJ*, 664, L111
- Españolat, C., et al., 2010, *ApJ*, 717, 441
- Españolat, C., et al., 2012, *ApJ*, 747, 2
- Españolat, C., et al., 2014, in *Protostars and Planets VI*
- Fang, M., et al., 2013, *A&A*, 549, 15
- Fazio, G., et al., 2004, *ApJS*, 153, 39
- Fedele, D., van den Ancker, M. E., Henning, T., Jayawardhana, R., & Oliveira, J. M. 2010, *A&A*, 510, A72
- Flaherty, K., et al., 2007, *ApJ*, 663, 1069
- Flaherty, K., Muzerolle, J., 2008, *AJ*, 135, 966
- Forbrich, J., et al., 2008, *ApJ*, 687, 1107
- Gutermuth, R., et al., 2004, *ApJS*, 154, 374
- Gutermuth, R., et al., 2008, *ApJS*, 674, 336
- Gutermuth, R., et al., 2009, *ApJS*, 184, 18
- Haisch, K., Lada, E., Lada, C., 2001, *ApJ*, 553, L153
- Hartmann, L., Calvet, N., Gullbring, E., & D'Alessio, P. 1998, *ApJ*, 495, 385
- Hartmann, L., Megeath, S. T., Allen, L., et al., 2005, *ApJ*, 629, 881
- Hatzes, A. P., Guenther, E. W., Endl, M., et al. 2005, *A&A*, 437, 743
- Hernandez, J., et al., 2004, *AJ*, 127, 1682
- Hernandez, J., et al., 2005, *AJ*, 129, 856
- Hernandez, J., et al., 2006, *ApJ*, 652, 472
- Hernandez, J., et al., 2007a, *ApJ*, 662, 1067
- Hernandez, J., et al., 2007b, *ApJ*, 671, 1784
- Indebetouw, R., et al., 2005, *ApJ*, 619, 931
- Jayawardhana, R., et al., 2006, *ApJ*, 648, 1206
- Jeffries, R., et al., 2007, *MNRAS*, 376, 580
- Kenyon, S. J., Hartmann, L., 1987, *ApJ*, 323, 714
- Kenyon, S., Bromley, B., 2004, *ApJ*, 602, L133
- Kenyon, S., Bromley, B., 2008, *ApJS*, 179, 451
- Kenyon, S., Bromley, B., 2009, *ApJ*, 690, L140
- Knutson, H., et al., 2007, *Nature*, 447, 183
- Konopacky, Q., et al., 2013, *Science*, 339, 1398
- Kraus, A., Ireland, M., 2012, Hillenbrand, L., Martinache, F., *ApJ*, 745, 19
- Lada, C. J., et al., 2006, *AJ*, 131, 1574
- Lambrechts, M., Johansen, A., 2012, *A&A*, 544, 32L
- Lisse, C., et al., 2008, *ApJ*, 673, 1106
- Lisse, C., et al., 2009, *ApJ*, 701, 2019
- Low, F., et al., 2005, *ApJ*, 631, 1170
- Luhman, K. L., Allen, P. R., Espaillat, C., Hartmann, L., & Calvet, N. 2010, *ApJS*, 186, 111
- Luhman, K. L., Mamajek, E. E., 2012, *ApJ*, 758, 31
- Makovoz, A., 2005, *PASP*, 347, 81
- Mamajek, E., 2009, in *Exoplanets and Disks: Their Formation and Diversity*, Proceedings of the Subaru International Conference, Vol. 1158, pg. 3-10
- Marois, C., et al., 2008, *Science*, 322, 1348
- Marsh-Boyer, A., et al., 2012, *AJ*, 144, 158
- Mathews, G., et al., 2013, *A&A*, 558, 30
- Megeath, S. T., et al., 2005, *ApJ*, 634, L113
- Merin, B., et al., 2010, *ApJ*, 718, 1200
- Miller, G. E., & Scalo, J. M. 1979, *ApJS*, 41, 513
- Mohanty, S., et al., 2005, *ApJ*, 626, 498
- Muzerolle, J., et al., 2010, *ApJ*, 708, 1107
- Quijada, E., 2004, *SPIE*, 5487, 244
- Palla, F., Stahler, S., 1999, *ApJ*, 525, 772
- Papovich, C., et al., 2004, *ApJS*, 154, 70
- Pascucci, I., Gorti, U., Hollenbach, D., et al. 2006, *ApJ*, 651, 1177
- Pecaut, M., Mamajek, E., Bubar, E., 2012, *ApJ*, 746, 154
- Pecaut, M., Mamajek, E., 2013, *ApJS*, 208, 9
- Pollack, J., et al., 1996, *Icarus*, 124, 62
- Preibisch, T., et al., 2002, *AJ*, 124, 404
- Rieke, G., et al., 2004, *ApJS*, 154, 25
- Rieke, G., et al., 2005, *ApJ*, 620, 1010
- Rhee, J., et al., 2007, *ApJ*, 671, 616
- Roberge, A., et al., 2008, *ApJ*, 626, L105
- Robitaille, T., et al., 2006, *ApJS*
- Sicilia-Aguilar, A., et al., 2006, *AJ*, 638, 897
- Sicilia-Aguilar, A., et al., 2009, *ApJ*, 701, 1188
- Silverstone, M. D., Meyer, M. R., Mamajek, E. E., et al. 2006, *ApJ*, 639, 1138
- Skrutskie, M., et al., 1990, *AJ*, 99, 1187
- Skrutskie, M., et al., 2006, *AJ*, 131, 1163
- Slesnick, C., et al., 2002, *ApJ*, 576, 880
- Soderblom, D. R., Hillenbrand, L. A., Jeffries, R. D., Mamajek, E. E., & Naylor, T. 2014, arXiv:1311.7024
- Stern, D., et al., 2005, *ApJ*, 631, 163
- Strom, K. M., Strom, S. E., Edwards, S., Cabrit, S., & Skrutskie, M. F. 1989, *AJ*, 97, 1451
- Su, K. Y. L., et al., 2006, *ApJ*, 653, 675
- Thompson, T., 2013, *MNRAS*, 431, 63
- White, R., Basri, G., 2003, *ApJ*, 582, 1109
- Whitney, B., et al., 2003a, *ApJ*, 591, 1049
- Whitney, B., et al., 2003b, *ApJ*, 598, 1079
- Wolk, S., Walter, F., 1996, *ApJ*, 111, 2066
- Wyatt, M. C., 2008, *ARA&A*, 46, 339

those for Taurus (Mathews et al. 2013). They likely provide evidence for homologous depletion of disk material for most of the population (Mathews et al. 2013). Our own independent analysis

of Upper Sco targets shows evidence for a much larger transitional disk population.

APPENDIX

Expected Levels of Extragalactic Contamination of h and χ Persei Members

From our line of sight, h and χ Persei an extremely populous cluster projected out of the galactic plane by ~ 200 pc, and the Spitzer data reaches completeness limits of $\sim 51 \mu Jy$ at [8], making extragalactic contamination of at least one cluster member very likely. To assess the probable frequency of contamination as a function of wavelength and magnitude, we use the IRAC number counts derived for the Bootes field from Fazio et al. (2004) and the MIPS-24 μm counts derived from Papovich et al. (2004). In Fazio et al. (2004), the number counts are differential, estimating the number of galaxies per magnitude in half-magnitude bins¹⁶.

We estimate the frequency of galactic contamination using the following relation:

$$N_{contamination} = \pi \times r_m^2 \times N_g \times N_{star}/A, \quad (1)$$

where r_m is the matching radius ($1''$), N_g is the number of galaxies in a square degree, and N_{star} is the number of members in our survey area, A. Here, N_{star} is the subset of $\sim 13,960$ probable cluster members located within the IRAC/MIPS fields: $\approx 12,000$ for IRAC and ≈ 9600 for MIPS. The survey area covers ~ 0.5 square degrees in the IRAC 8 μm filter and 0.4 square degrees in MIPS-24.

From the IRAC 8 μm differential number counts at m(IRAC) = 14, 15, 15.5, and 16 yields, we then expect the following number of members contaminated by galaxies on our IRAC mosaics as a function of magnitude: ~ 4 , 9, 22, and 31 galaxies with magnitudes of m[8] = 14, 15, 15.5, and 16, respectively. The IRAC color-magnitude diagram for [8] vs. [3.6,4.5]-[8] implies that a member must have have [3.6,4.5]-[8] $\gtrsim 0.75$ to be flagged as an excess source for the faintest objects detected at 5- σ at [8]. Our faint detection limit is at m[8] ≈ 15.5 , so galaxies as faint as m[8] ~ 16.25 can contaminate a member, making it appear as bright as m[8] = 15.5 and giving it a [3.6,4.5]-[8] color $\gtrsim 0.75$. Thus, galaxies in the m[8] = 16 bin (m[8] = 15.75-16.25) are the faintest ones that could possibly contaminate a member's photometry. Summing from m[8] = 12 to 15.5 (16), we expect 47 (78) members to have IRAC photometry contaminated by a galaxy.

The density of galaxies brighter than [24] = 11.25 is expected to be $\sim 10^7 \text{ sr}^{-1}$ (cf. Papovich et al. 2004). Over our 0.4 square-degree MIPS area, we expect ~ 1200 galaxies brighter than this limit. Adopting $N_{star} = 9600$ and an area of A = 0.4 sq. deg., we predict that 18 members are contaminated from galaxies brighter than [24] = 11.25. As depicted in Figure 6, the number of excess sources at 8 and 24 μm is significantly larger than the number of expected extragalactic contaminants.

Extragalactic Contamination of the h and χ Persei IRAC/MIPS Excess Population

Not all galaxies measurably affect the observed mid-IR colors of the stars they contaminate if the stars are much brighter than the galaxies in the IRAC bands, as many have near zero IRAC color (see Fig. 1 in Stern et al. 2005). However, broad-line active galactic nuclei (BL-AGN) and PAH-emission galaxies both have very red IRAC colors (Gutermuth et al. 2008). Member contamination by these galaxies can mimick the presence of a disk. Here we compare the distribution of IRAC colors for members to those expected for BL-AGN and PAH-emission galaxies using color-color diagrams as in Gutermuth et al. (2008, 2009).

Active star-forming galaxies (e.g. broad-line AGN) have very red [5.8]-[8] colors due to strong PAH emission. Gutermuth et al. (2008, 2009) define regions in [4.5]-[5.8]/[5.8]-[8] and [3.6]-[5.8]/[4.5]-[8] diagrams where these galaxies reside and removed objects located within as contaminants. We first focus on PAH-emission galaxies, definig the region of likely PAH-emission galaxy contamination as follows:

$$\begin{aligned} [5.8] - [8] &\geq 1.5 \\ [4.5] - [5.8] &\leq 3 \times ([5.8] - [8] - 1.5) \\ [4.5] - [8] &\geq 1.7 \\ [3.6] - [5.8] &\leq (2/1.3) \times ([4.5] - [8] - 1.3). \end{aligned}$$

Compared to the criteria in Gutermuth et al. (2008, 2009), our adopted colors for PAH-emission galaxies are ~ 0.5 and 0.7 magnitudes redder in [5.8]-[8] and [4.5]-[8]. However, they cover all of the Bootes-field PAH galaxies shown in Gutermuth et al. and thus should be acceptable for targeting this specific type of contaminant.

To compare our member colors to those expected from AGN contaminants, we simply adopt the boundaries listed in Stern et al. (2005):

$$\begin{aligned} [5.8] - [8] &\geq 0.6 \\ [3.6] - [4.5] &\geq 0.2 \times ([5.8] - [8]) + 0.18 \\ [3.6] - [4.5] &\geq 2.5 \times ([5.8] - [8]) - 3.5. \end{aligned}$$

Gutermuth et al. (2008, 2009) do not flag AGN from color-color diagrams because the IRAC colors of AGN exhibit very strong overlap with young stellar objects in *color-color diagrams* but exhibit much weaker overlap with the

¹⁶ Thus the differential number counts at m[IRAC] = 15.5 are defined from galaxies with m[IRAC] = 15.25–15.75. To compute

the number of galaxies expected with m[IRAC]=15.25–15.75, we must multiply by the bin width of 0.5 magnitudes.

TABLE 1
LIST OF CANDIDATE/PROBABLE H AND χ PERSEI MEMBERS (REVISED FROM CURRIE ET AL. 2010)

Member ID Number	Photometry Running Number	Spectroscopy Running Number	Membership Type	RA	DEC	Numerical Spectral Type	V	$\sigma(V)$	I	$\sigma(I_c)$
1	3	174	1	34.7691	57.1355	13.0	7.1731	0.0001	6.6876	0.0001
2	16	60	3	34.6173	57.2084	11.5	7.7866	0.0001	7.3575	0.0001
3	17	11	3	34.5962	57.0102	10.7	7.8288	0.0001	7.4510	0.0001
4	30	8	3	34.4577	57.0904	10.5	8.0183	0.0001	7.5970	0.0001
5	39	69	3	34.6996	57.0673	11.5	8.2215	0.0001	7.6884	0.0001

NOTE. — The membership type has the following meaning: Candidate members identified from 1 = Photometry, 2 = Spectroscopy 3 = Spectroscopy and Photometry. A zero for either the photometry or spectroscopy running number means that the source lacks either optical photometric or spectroscopic data. The spectroscopy running number corresponds to the running number from the combined photometry + spectroscopy table (Table 3), not the running number from Table 2. The optical photometry listed here comes from that obtained in Currie et al. (2010), which may be saturated for the brightest stars.

TABLE 2
PHOTOMETRY FOR CANDIDATE/PROBABLE H AND χ PERSEI MEMBERS

ID	RA	DEC	SpT	V	$\sigma(V)$	[3.6]	$\sigma([3.6])$	[4.5]	$\sigma([4.5])$	[5.8]	$\sigma([5.8])$	[8]	$\sigma([8])$	[24]	$\sigma([24])$
2	34.6173	57.2084	11.5	7.7866	0.0001	7.480	0.002	7.475	0.002	7.427	0.002	7.415	0.001	7.339	0.047
3	34.5962	57.0102	10.7	7.8288	0.0001	7.974	0.003	7.974	0.003	7.975	0.002	7.967	0.001	7.861	0.038
4	34.4577	57.0904	10.5	8.0183	0.0001	8.260	0.002	8.248	0.002	8.203	0.002	8.210	0.001	8.187	0.032
5	34.6996	57.0673	11.5	8.2215	0.0001	7.979	0.002	7.881	0.002	7.717	0.001	7.578	0.001	6.659	0.031
7	34.7002	57.2855	12.0	8.3787	0.0001	8.569	0.002	8.583	0.002	8.570	0.002	8.552	0.002	8.505	0.048

NOTE. —

color-magnitude diagram positions of YSOs. The situation here is reversed. Using here the color-magnitude diagram criteria they adopt would flag as an AGN nearly every single h and χ Persei member with an IRAC excess. However, by adopting the Stern et al. (2005) color-color criteria we can neatly separate h and χ Persei stars from strong AGN contamination.

Figure 19 compares the IRAC colors of all objects on the h and χ Persei field (left panels) and cluster members only (right panels) with the predicted colors of PAH-emission galaxies and AGN. Numerous IRAC-detected objects on the field exhibit colors indicative of extragalactic contaminants according to our criteria and to Gutermuth et al.'s. However, contamination is essentially absent when we restrict our analyses to previously identified cluster members. Our criteria fails to find any members strongly contaminated by PAH-emission galaxies and only two with colors consistent with AGN contamination. We likewise find no such objects in [4.5]-[5.8] vs. [5.8]-[8] diagrams (not shown), and we would fail to find such objects as long as the blue limit in [4.5, 5.8]-[8] is redder than 1.2. Adopting Gutermuth et al.'s criteria, we identify five objects with colors only marginally consistent with PAH-emission galaxy contamination.

Thus, while we cannot prove that no cluster member has IRAC excess emission due to extragalactic contamination, we fail to find evidence for anything more than a negligible population of *strongly* contaminated members. The 47–78 members predicted to be contaminated by galaxies then generally are either much brighter than the contaminating galaxies themselves or are contaminated by galaxies with intrinsic IRAC colors near zero (e.g. not PAH-emission galaxies or BL-AGN).

TABLE 3
MAPPING BETWEEN OBSERVED AND INTRINSIC PROPERTIES FOR η
AND χ PERSEI STARS

Stellar Mass (M_{\odot})	T_{eff} (K)	SpT (Cu10a)	SpT (P13)	V_{obs}
6.0	19950	12.5/12	12.25	11.8
5.0	16900	14/13	14	12.8
4.0	14790	15.5	16	13.3
3.5	13400	17	17.5	14.2
3.0	12100	18	18	14.3
2.5	10900	19	19	14.6
2.0	9300	21.5	21	15.2
1.5	7210	30	30	16.2
1.4	6402	35	35.5	16.5
1.3	5750	45	42.5	17.4
1.2	5218	50	50.5	18.3
1.1	4794	53	53	19.0
1	4470	54.5	55	19.7
0.95	4326	55	55.5	20.1
0.9	4185	56	56	20.4
0.8	3961	57.5	58	21.1
0.7	3811	60.5	60.5	21.6
0.6	3694	61.5	61	22.1
0.5	3693	61.5	61	22.6
0.4	3452	63	62.5	23.1

NOTE. — For 1.5–6 M_{\odot} stars we use Palla and Stahler (1999) to map between intrinsic and observable properties. For lower-mass stars, we use Baraffe et al. (1998). For comparison with our spectral type/ T_{eff} conversions, we list the spectral types from Pecaut and Mamajek (2013), which show excellent agreement for nearly every entry.



FIG. 1.— Multicolor mosaic image centered on η and χ Persei. Blue identifies emission from the 3.6 μm filter, green from the 4.5 μm filter, and red from the 8 μm filter. The core of η Persei is centered on the overdense region of stars at the middle-right; the χ Persei core is identified by an M supergiant at the middle-left.

TABLE 4
CANDIDATE ACCRETING STARS

RA	DEC	ST	$EW(H_\alpha)$	[3.6]-[8]	[4.5]-[8]
35.8788	56.9368	43.4	-5.60	-99.000	0.010
34.8733	57.0952	45.0	-19.30	0.084	0.051
34.8106	56.8745	62.9	-6.50	0.114	0.031
34.7858	57.1891	39.8	-3.30	0.088	0.037
34.7723	57.1504	40.7	-6.50	-0.088	-0.084
34.8196	57.4537	40.8	-1.30	-0.178	-0.193
34.8565	57.1389	41.3	-12.60	0.068	0.054
34.8455	57.1830	62.8	-5.30	-0.423	-0.535
34.8293	57.2154	47.2	-2.10	0.519	0.460
35.9386	57.2865	44.6	-2.20	-0.123	-0.115
34.8521	57.0314	46.4	-21.30	0.119	-0.042
34.9686	56.9170	42.4	-0.80	-99.000	-99.000
36.2416	57.3407	42.7	-4.20	-99.000	-99.000
36.1889	57.4141	52.8	-82.90	-99.000	-99.000
35.9331	57.3837	54.0	-43.10	-99.000	-99.000
36.1516	57.4623	45.5	-6.20	-99.000	-99.000
35.7826	56.9684	50.8	-19.10	0.052	0.061
35.5140	57.1173	42.2	-20.00	-0.049	-0.065
35.8746	57.3021	48.7	-8.10	0.066	0.064
34.9739	57.0482	43.4	-8.30	-0.011	-99.000
36.1228	57.3046	42.2	-10.10	-99.000	-99.000
35.4319	56.8294	53.3	-17.20	0.058	0.057
35.0511	57.1230	43.5	-0.50	0.272	0.255
34.8044	57.2098	40.0	-7.70	0.133	0.093
34.7157	57.1875	43.2	-7.00	-99.000	-99.000
35.0980	57.0256	42.6	-7.00	-0.027	-0.024
34.7179	57.0764	47.0	-16.10	-0.129	-0.180
34.6226	57.5886	64.5	-6.80	-99.000	-99.000
35.0717	57.1476	44.2	-0.70	-0.045	-0.081
34.8229	57.1354	38.2	-1.40	0.040	0.016
34.9248	57.3163	45.6	-7.40	0.161	0.176
35.5106	57.0000	45.1	-11.80	-0.023	-0.027
34.8816	57.0840	38.9	0.70	0.198	0.242
34.3993	56.8156	51.7	-25.00	-99.000	-99.000
34.5443	57.0386	45.1	0.80	-99.000	-99.000
34.8499	57.0401	44.4	-0.50	0.063	0.122
35.1955	56.8353	41.8	-8.30	-0.039	-0.059
35.9421	57.2128	18.8	7.10	0.183	0.173
34.8515	57.0719	52.6	-5.30	0.500	0.512
34.7243	57.1288	36.6	-6.20	-99.000	-99.000
34.6675	57.1491	43.0	-11.10	0.159	0.180
35.9057	56.7800	39.5	-1.20	-99.000	-99.000
35.5901	57.0668	44.1	-13.74	0.184	0.159
35.6647	57.2619	40.2	-4.50	0.011	-99.000
34.4040	57.0196	40.5	-1.80	-0.103	-0.107
34.4798	56.9342	42.7	-6.46	0.101	0.079
35.4435	57.0456	44.2	-5.75	0.033	0.017
35.5172	57.3804	39.0	-3.40	0.191	0.145
35.0596	56.7393	40.9	-12.40	-99.000	-99.000
35.2182	57.2180	46.0	-8.50	-0.071	-0.026
35.8477	57.0570	40.2	-3.20	0.240	0.196
34.5238	57.3162	41.6	-15.42	-99.000	-0.015
34.5224	57.0245	42.5	-10.15	0.041	0.012
35.1531	57.0935	42.4	-8.98	-0.011	-0.029
35.8870	57.1159	45.0	-8.60	0.147	0.083
34.2805	57.1869	44.1	-9.79	0.063	-0.085
35.6276	57.2429	47.3	-12.93	0.133	0.098
35.7026	57.2102	48.0	-7.90	0.297	0.258
35.4154	57.2804	44.6	-12.74	-0.044	-0.072
35.6574	57.2178	39.8	-2.86	-0.150	-0.177
35.5286	57.1292	50.7	-13.07	0.140	0.124
35.3857	57.0089	40.4	-5.00	-0.057	-0.111
35.4009	57.1858	42.2	-23.00	-0.023	-99.000
35.4913	57.0680	50.0	-12.96	0.149	0.104
34.7779	56.8716	50.6	-8.80	0.205	0.150
35.3994	57.0897	51.1	-29.93	0.060	0.052
34.4520	57.3922	51.6	-19.40	-99.000	-99.000
34.6519	57.0209	46.0	-11.59	0.126	0.179
35.3151	57.0772	52.5	-26.40	0.017	-99.000
34.4112	57.4461	53.9	-59.50	-99.000	-99.000
34.5489	57.0786	57.4	-47.32	0.678	0.431
34.6662	57.1706	25.0	0.00	0.078	0.056

NOTE. — The numerical spectral type has the following formalism: 10=B0, 11=B1 ... 68=M8. The **Source** column refers to the source of the spectroscopic data: Hectospec (1), Hydra (2), or FAST (3). **Archive Number** refers to the numerical suffix as stored in the spectral archive at the Center for Astrophysics' *Telescope Data Center*, as described in Currie et al. (2010). The equivalent widths of H_α and H_β are listed in units of angstroms. Spitzer/IRAC photometry at [3.6] and [8] are from this paper.

TABLE 5
PROPERTIES OF MODELED DISK-BEARING H AND χ PERSEI STARS

α	δ	SpT	E(B-V)	SpT est.	E(B-V) est.	[3.6]-[8]	[4.5]-[8]	[3.6]-[24]	[4.5]-[24]	R_{disk}/R_{sub}	Disk Type
34.4833	57.1675	A7.4	0.572	-	-	0.133	0.116	2.077	2.060	6	TDHD/WDD
34.5675	57.0963	B8.5	0.673	-	-	0.618	0.433	1.758	1.573	400	TDHD/WDD (TDIH)
34.6778	57.0202	-	-	M2	0.650	1.126	1.081	4.056	4.012	20	TDIH
34.7561	57.0997	-	-	K0	0.650	0.250	0.225	1.900	1.875	1	TDHD/WDD
34.7786	57.0364	G5.2	0.848	-	-	0.412	0.244	3.514	3.345	1	TDHD/WDD
34.7824	57.2346	F8.3	0.582	-	-	1.239	1.157	4.232	4.150	10	TDHD/WDD
34.9145	57.4071	F5.1	0.605	-	-	0.709	0.665	2.684	2.639	1	TDHD/WDD
34.9447	57.1925	G1.1	0.675	-	-	1.004	0.929	5.230	5.154	40	TDIH
35.0298	57.1013	-	-	M4	0.700	0.998	0.905	4.129	4.035	20	TDIH
35.0501	57.0758	-	-	M1	0.700	1.859	1.261	4.742	4.144	8	PD
35.1028	56.8800	-	-	K0	0.500	0.368	0.447	2.203	2.282	1	TDHD/WDD
35.3153	57.2595	-	-	A5	0.300	0.199	0.178	1.564	1.544	30	TDHD/WDD (TDIH)
35.4073	57.0433	-	-	K7	0.520	0.592	0.474	4.805	4.686	300	TDIH
35.4106	56.9030	F5.9	0.474	-	-	1.391	1.224	4.706	4.539	20	TDHD/WDD (TDIH)
35.6905	56.9388	-	-	M5	0.520	0.948	0.803	5.266	5.121	15	TDIH
35.6914	57.2379	-	-	K7	0.520	0.874	0.822	3.816	3.764	1	TDHD/WDD
35.6923	56.9258	-	-	M0	0.560	0.751	0.620	4.518	4.386	30	TDIH
35.8256	56.8723	-	-	M5	0.700	-99.	1.533	-99.	5.167	30	PD (TDIH)

NOTE. — Observed properties of 8 μm and 24 μm excess sources in h and χ Persei. Dashes indicate that a value was not applicable to that specific column. The final entry does not have a 3.6 μm detection, this is indicated with a value of -99. for its computed colors involving [3.6]. R_{disk}/R_{sub} denotes the disk inner radius in units of the disk sublimation radius derived from fitting the source SED with the Robitaille et al. radiative transfer model grid. Sources with inner holes have a best-estimated inner disk radius of $R_{disk} > 10 \times R_{sub}$. The disk classification (right-most column) is determined by comparing source SEDs with the fiducial disk model: PD = primordial disk, TDIH = a transitional disk with an inner hole, and TDHD/WDD = a homologously depleted transitional disk or a warm debris disk. If SED model fitting from the Robitaille et al. (2006) grid favors a different classification, we put that alternate classification in parentheses.

TABLE 6
FREQUENCIES OF WARM CIRCUMSTELLAR DUST AND GAS FROM SPITZER SURVEYS

Name	Nominal Age (Myr)	Revised Age (Myr)	Disk Fraction	Accretion Fraction	References
NGC 1333	1	-	0.83 ± 0.11	-	1
ρ Oph	1	-	-	0.50 ± 0.16	2
Taurus	1.5	-	0.63 ± 0.09	0.59 ± 0.09	2,3
NGC 7129	1.5	-	0.54 ± 0.14	-	4
NGC 2068/71	2	-	-	0.61 ± 0.09	5
Cha I	2	-	-	0.44 ± 0.08	2
IC 348	2.5	6	0.47 ± 0.12	0.33 ± 0.06	2,6
σ Orionis	3	$6^{+7.4}_{-1.3}$	0.36 ± 0.04	0.30 ± 0.05	7,8
NGC 6231	3	-	-	0.15 ± 0.05	8
Tr37	3.5	-	0.48 ± 0.05	-	9
NGC 2362	5	$12^{+3.3}_{-4.1}$	0.20 ± 0.03	0.05 ± 0.05	10,11
Upper Sco	5	10	0.19 ± 0.05	0.07 ± 0.02	2,12
OB1b	5	-	0.17 ± 0.04	-	13
η Cha	6	-	0.40 ± 0.14	0.27 ± 0.19	14, 15
NGC 6531	7.5	-	-	0.08 ± 0.05	8
TWA	8	-	-	0.06 ± 0.06	15
25 Orionis	8.5	-	0.06 ± 0.023	0.06 ± 0.02	7,16
NGC 2169	9	-	-	$0.0^{+0.03}$	17
NGC 7160	11.8	$12.6^{+1.3}_{-2.1}$	0.04 ± 0.04	0.02 ± 0.02	9
β Pic MG	12	-	-	$0.0^{+0.13}$	15
h and χ Persei	14	-	0.022 ± 0.002	0.017 ± 0.003	This work
Tuc-Hor	27	-	-	$0.0^{+0.08}$	15
NGC 6664	46	-	-	$0.0^{+0.04}$	8

NOTE. — Nominal ages, revised ages from Bell et al. (2013) with empirical disk and accretor fractions for the clusters in Fig. 15. References: 1) Gutermuth et al. (2008), 2) Mohanty et al. (2005), 3) Hernandez et al. (2007a), 4) Gutermuth et al. (2004), 5) Flaherty and Muzerolle (2008), 6) Lada et al. (2006), 7) Hernandez et al. (2007b), 8) Fedele et al. (2010), 9) Sicilia-Aguilar et al. (2006), 10) Dahm and Hillenbrand (2007), 11) Currie et al. (2009), 12) Carpenter et al. (2006), 13) Hernandez et al. (2005), 14) Megeath et al. (2005), 15) Jayawardhana et al. (2006), 16) Briceno et al. (2007), 17) Jeffries et al. (2007), 18) this work

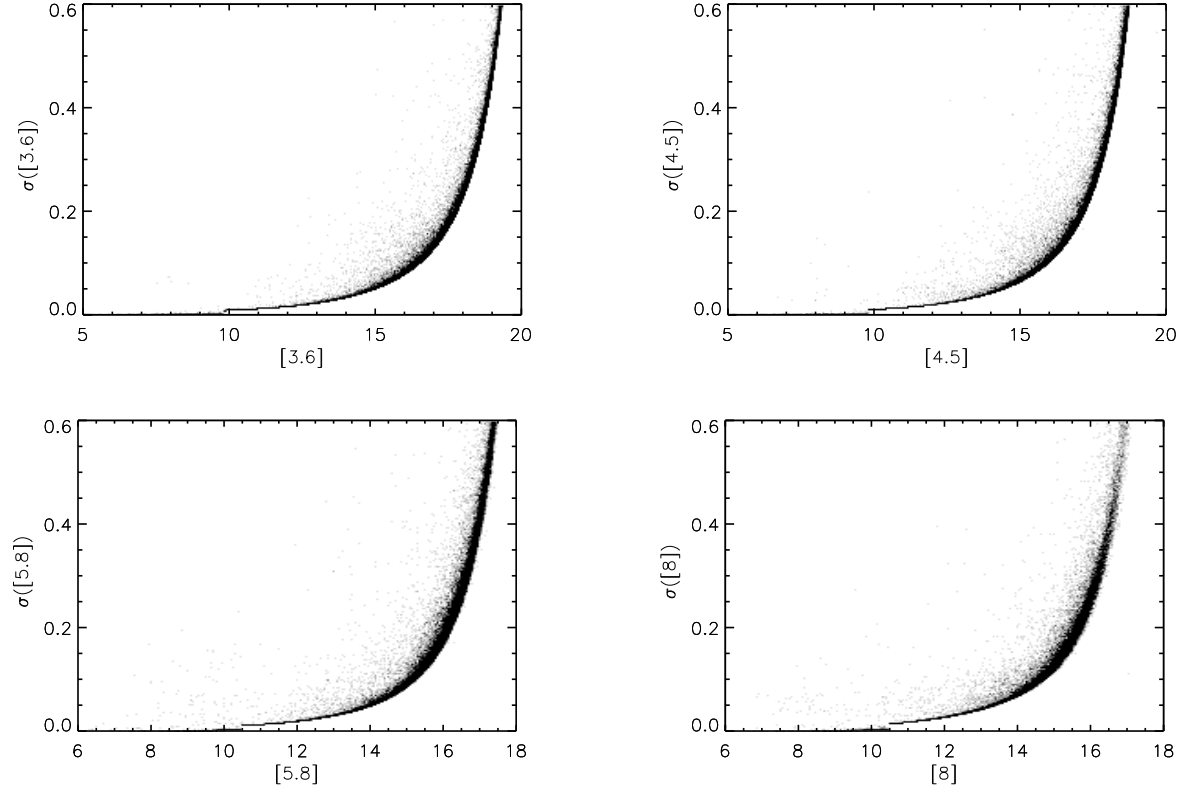


FIG. 2.— Density plot of the magnitude vs. error distribution for IRAC data.

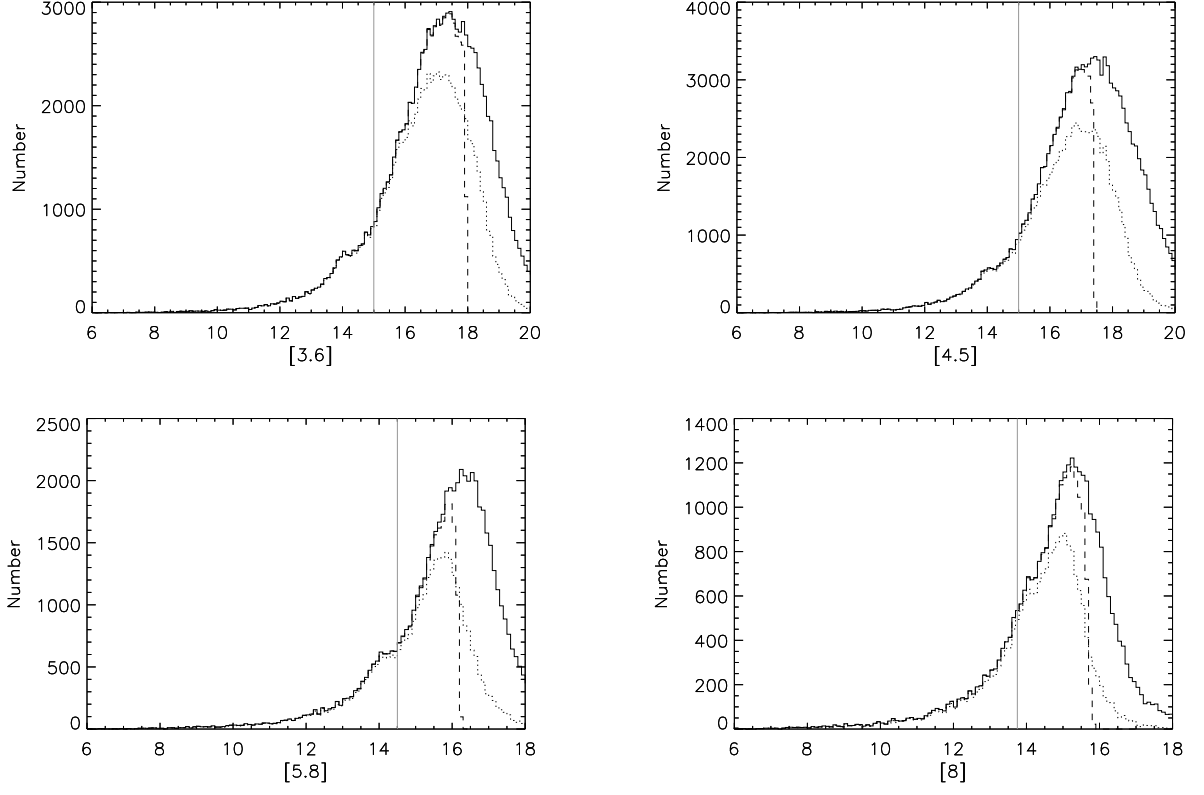


FIG. 3.— Number counts in the IRAC bands. The solid black lines identify all candidate detections, the dashed lines identify 5σ detections, and the dotted lines identify confirmed point sources (those with detections in multiple bands). The grey vertical lines identify where the source counts peak in Cycle 1 data presented by Currie et al. (2007a).

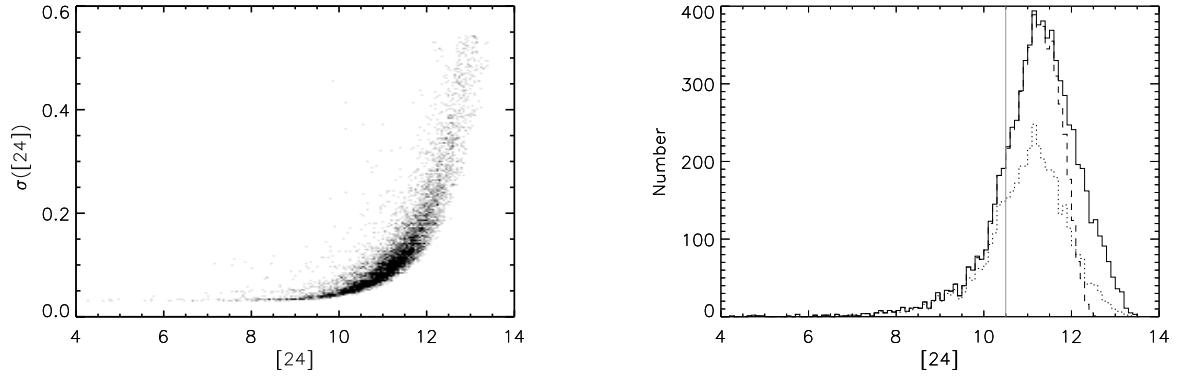


FIG. 4.— Density plot of the magnitude vs. error distribution (left) and number counts (right) for MIPS $24\ \mu\text{m}$ data. Symbols are the same as in Figures 1 and 2. The grey vertical line identifies where the source counts peak in data presented in Currie et al. (2008a).

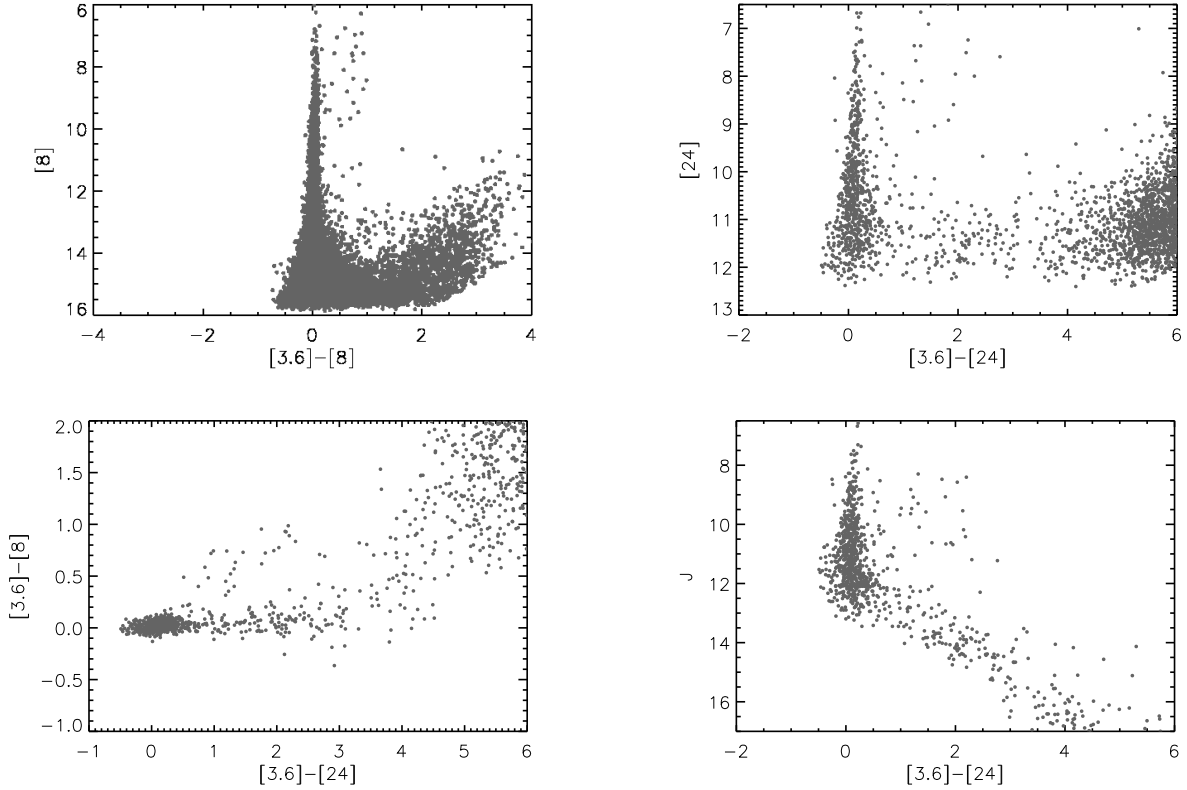


FIG. 5.— IRAC/MIPS color-magnitude and color-color diagrams for objects detected in multiple bandpasses. (Top-left) $[8]/[3.6]-[8]$ diagram showing a well-defined main locus of objects with \sim zero color, a population of weak, 0.25–1.5 magnitude excesses and a dense population of objects with red colors ($[3.6]-[8] \sim 1.5-4$). (Top-right) $[24]/[3.6]-[24]$ diagram showing more clearly the same three major populations: objects with zero color, a small weak-excess population ($[3.6]-[24] \sim 0.5-4.5$) and a dense strong-excess population ($[3.6]-[24] \gtrsim 4.5$). (Bottom-left) $[3.6]-[8]/[3.6]-[24]$ diagram showing that the objects with the strongest excesses in IRAC likewise have strongest excesses in MIPS, while those with $[3.6]-[24] \sim 0.5-4.5$ include objects with and without IRAC excesses. (Bottom-right) $J/[3.6]-[24]$ diagram showing that we only detect objects with zero $[3.6]-[24]$ color down to a 2MASS J magnitude limit of $\sim 12.5-13$.

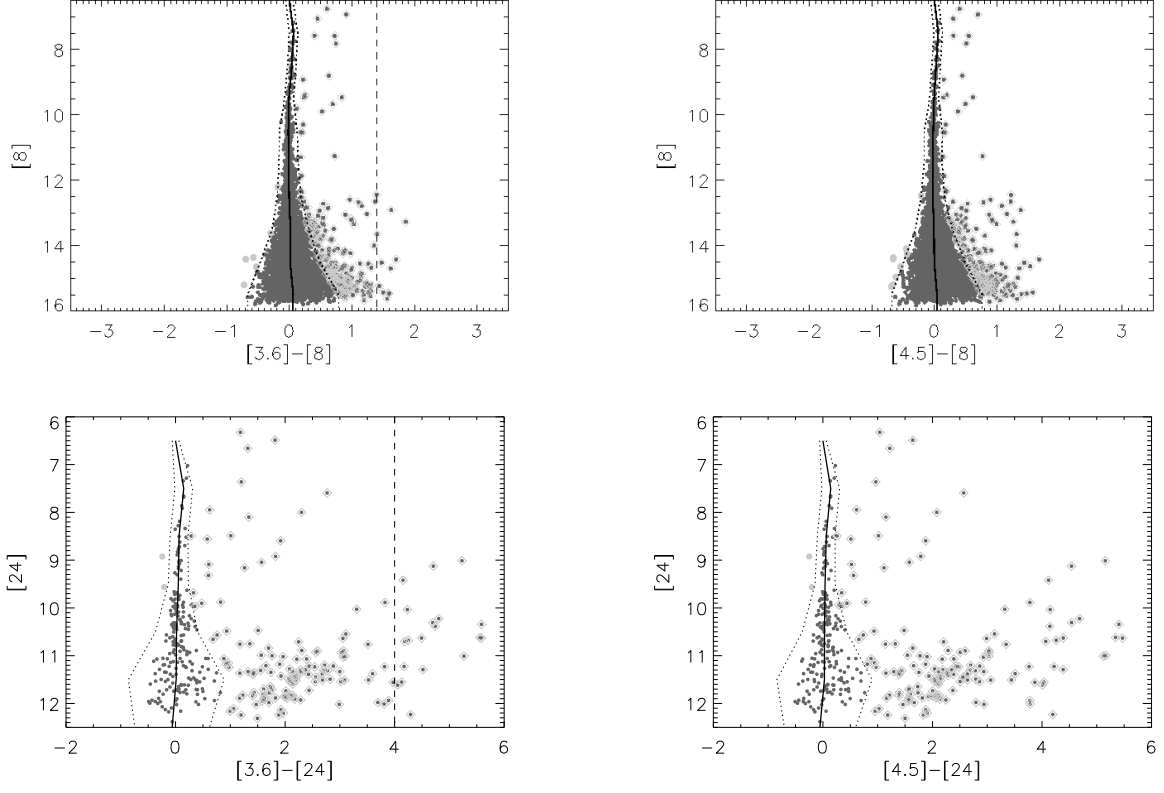


FIG. 6.— Color-magnitude diagram identifying IR excess sources (diamonds) and negative outliers (grey dots) compared to the full distribution of h and χ Persei sources. The solid lines identify the median color for a given [8] or [24] magnitude and the dashed lines separate objects whose colors are consistent with bare photospheres in a given passband and those deviant from this distribution by more than $\sim 3\sigma$. The vertical dashed lines in the top-left and bottom-left panels depict the typical colors for blue protoplanetary disks in Taurus drawn from Figure 5 in Luhman et al. (2010).

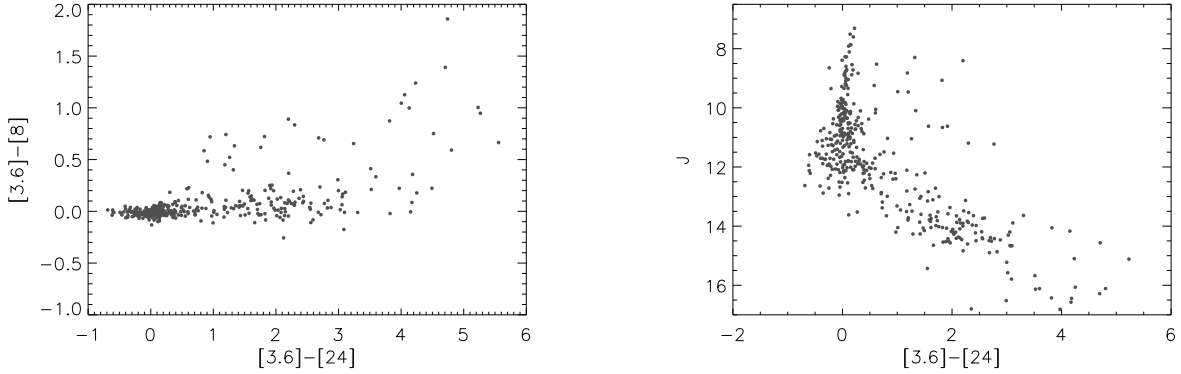


FIG. 7.— Same as Figure 5 (bottom panels) except just for h and χ Persei members.

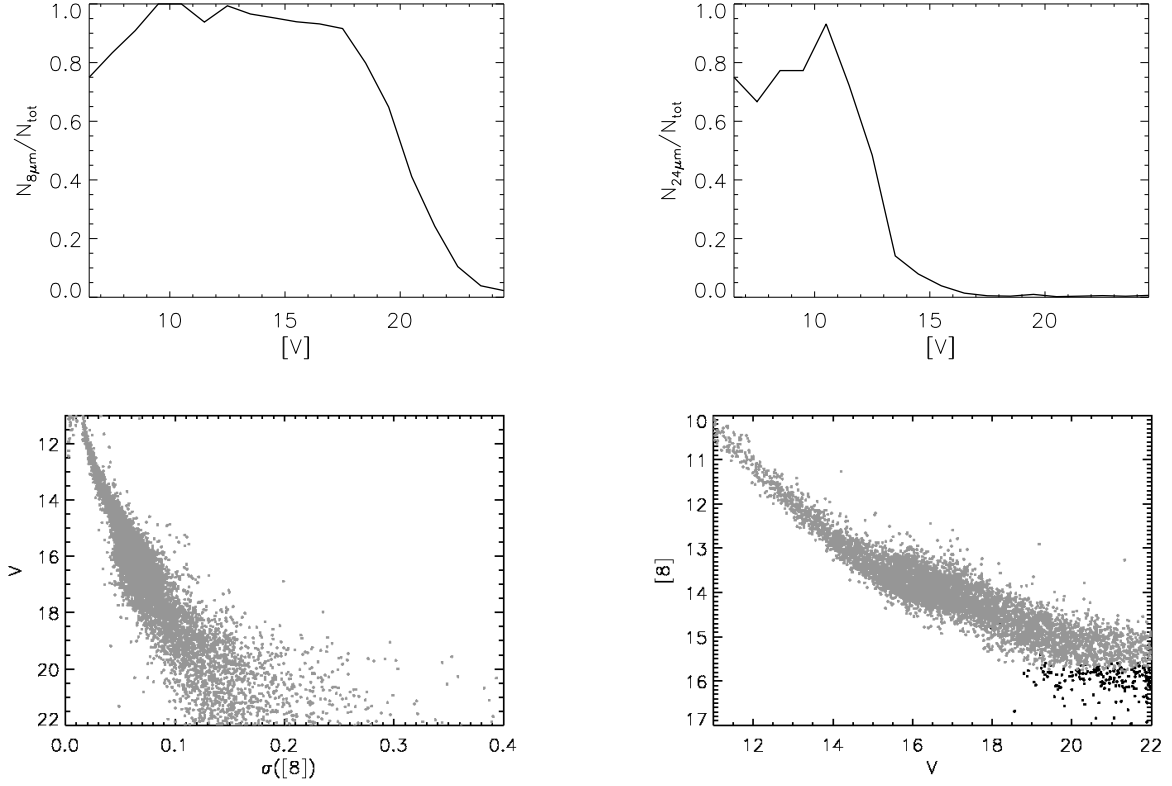


FIG. 8.— (Top) Completeness at [8] and [24] for cluster members. We restrict our statistical analysis to stars with $V \leq 22$ at $8\ \mu\text{m}$ and $V < 13$ at $24\ \mu\text{m}$. (Bottom) V vs $\sigma([8])$ and V vs. $[8]$ for our sample. In the righthand panel, the light grey dots identify stars with 5- σ [8] detections. Nearly all stars with lower signal-to-noise ratios are fainter than $[8] = 15.5$.

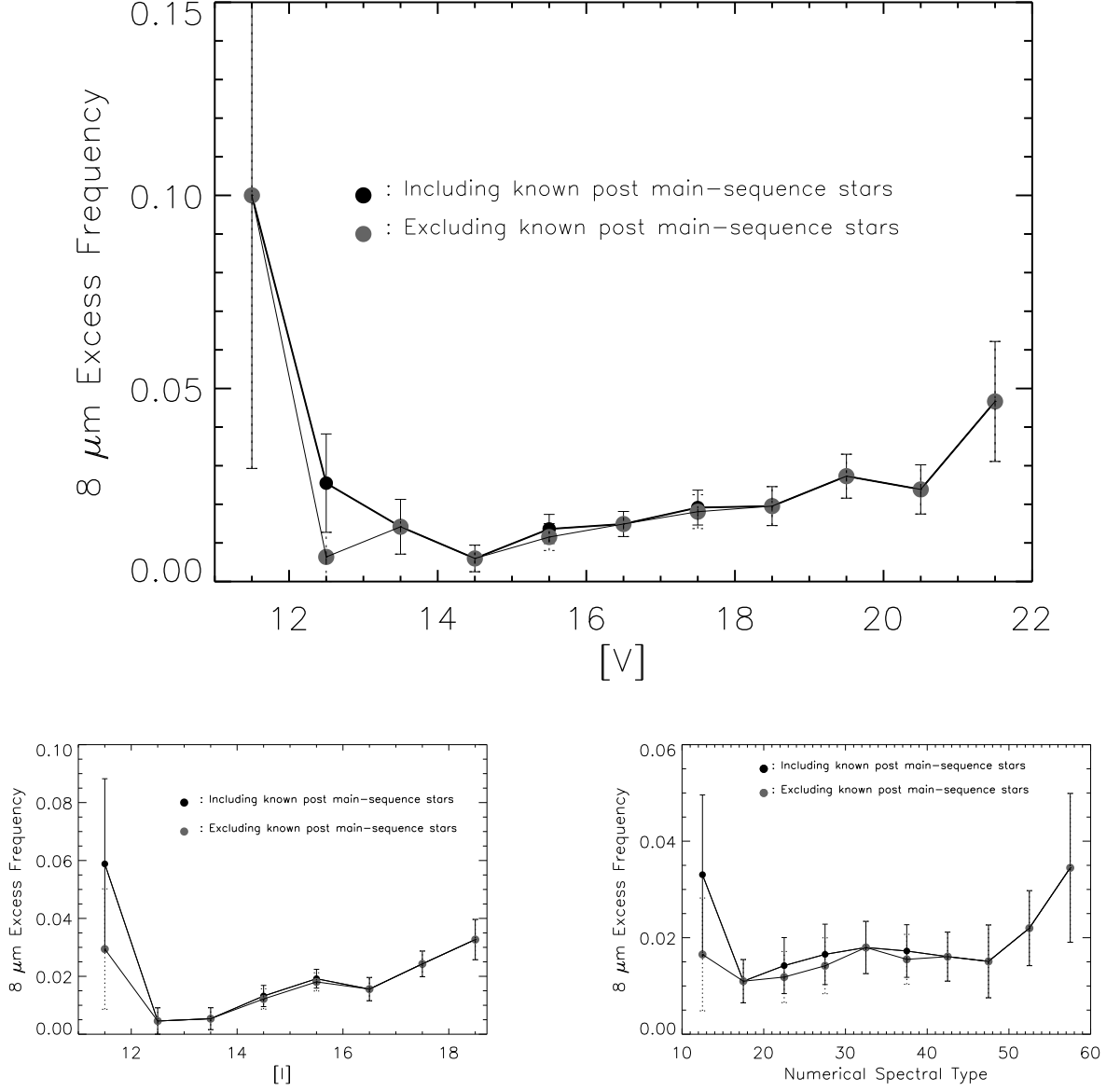


FIG. 9.— Frequency of 8 μm excess emission from disks vs. V -band magnitude (top), I -band magnitude (bottom-left), and (numerical) spectral type (bottom-right). As described previously, the numerical spectral type has the following formalism: 10=B0, 11=B1, ... 68=M8. In all plots, report frequencies including and excluding post-main sequence stars like giants and Be stars whose excess emission is likely not indicative of planet formation.

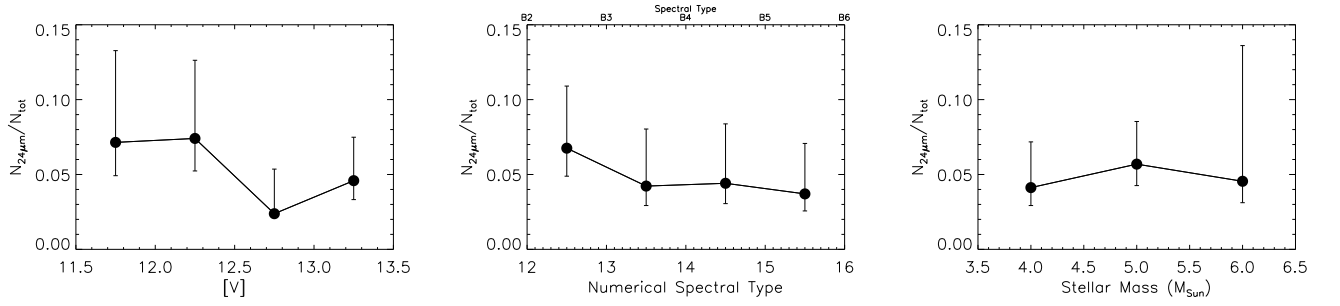


FIG. 10.— (Left) Frequency of h and χ Persei stars with MIPS-24 μm excess as a function of V -band magnitude (left), spectral type (middle), and inferred stellar mass (right). About 5% of the 4–6 M_{\odot} h and χ Persei stars show evidence for 24 μm excess.

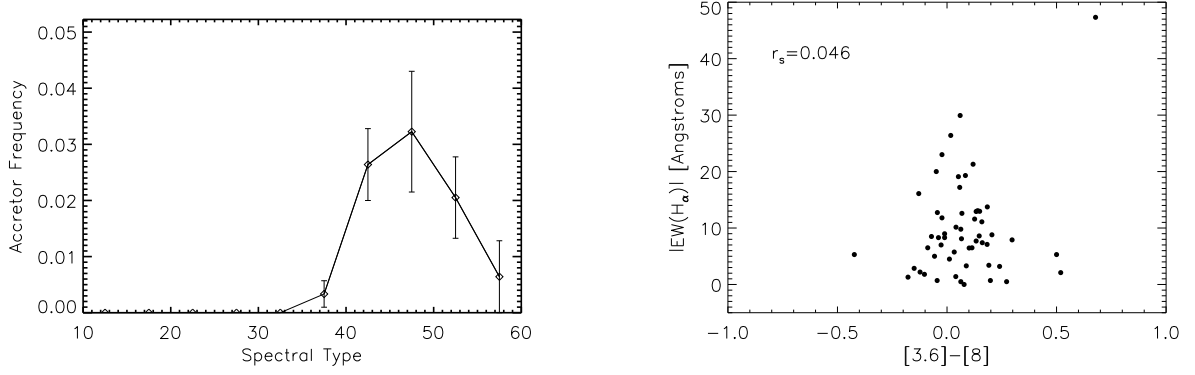


FIG. 11.— (Left) Frequency of accreting h and χ Persei stars as identified from their H_α equivalent widths. (Right) The H_α equivalent width vs. the [3.6]-[8] color, showing that there is no clear correlation between accretion diagnostics and those of warm circumstellar dust.

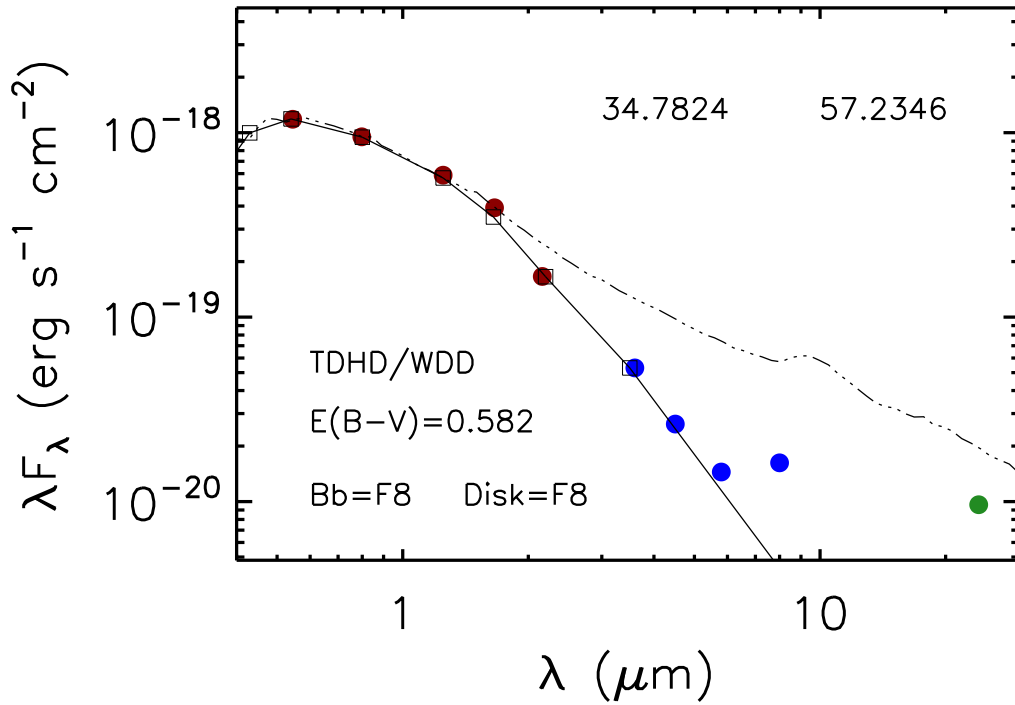


FIG. 12.— Sample spectral energy distribution a for h and χ Persei star with clear excesses in IRAC and MIPS bandpasses compared to photometric predictions for a bare stellar photosphere (solid line) and an optically-thick, flat reprocessing disk (dashed line). This object was previously identified as a terrestrial zone (warm) debris disk candidate from Currie et al. (2007b).

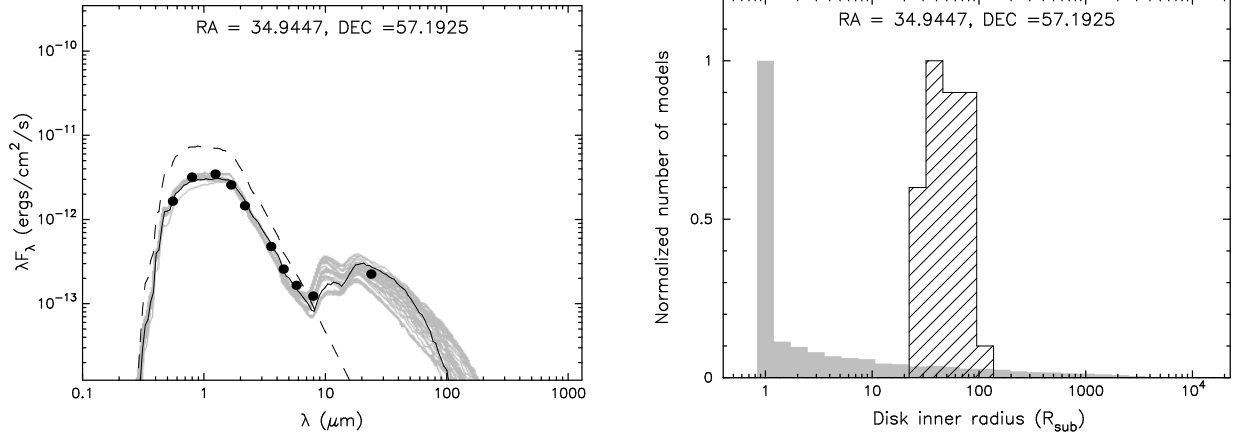


FIG. 13.— Sample SED modeling results using the Robitaille et al. grid. The left panel displays the set of best-fitting SED models. The right panel displays the distribution of disk inner radii (in units of the dust sublimation radius) for these SED models. For most of our modeled targets, the inferred disk classifications agree with our analysis based on fiducial comparisons. For this object and 3 others, SED modeling favors reclassifying the disks as having inner holes.

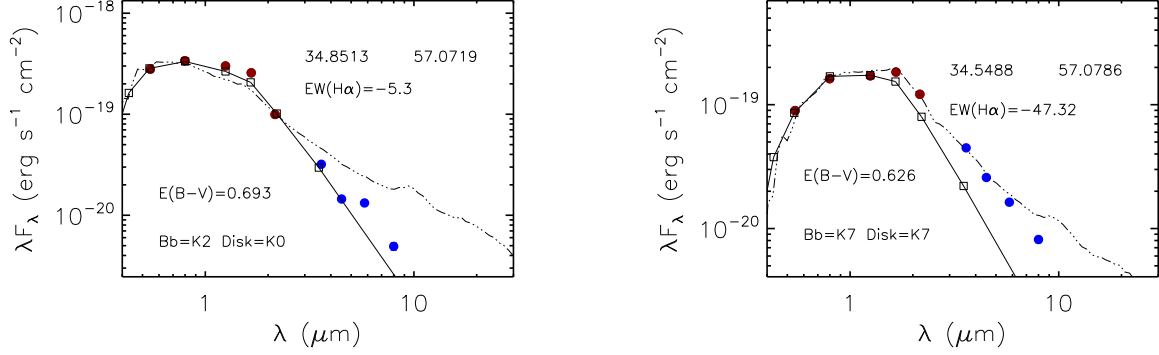


FIG. 14.— SEDs of two likely h and χ Persei members with $H\alpha$ emission indicative of circumstellar gas accretion. The differences in spectral types adopted for the model stellar photosphere (BB) and disk (“Disk”) reflect our sampling of the disk model grid: they do not affect our interpretation of either object.

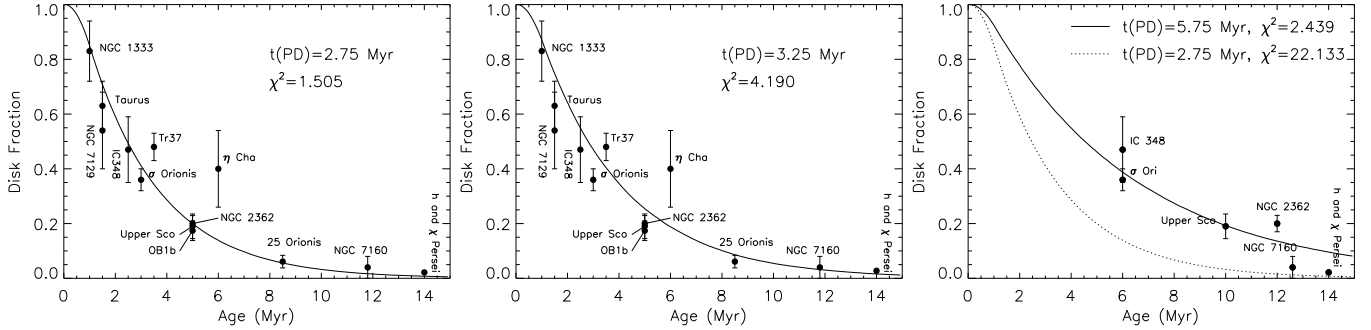


FIG. 15.— Frequency of warm circumstellar dust vs. time for h and χ Persei and many 1–20 *Myr*-old clusters/associations for nominal cluster ages (left/middle) and for clusters with revised ages from Bell et al. (2013) (right). In the left and right panels, the solid line depicts the best-fit timescale to the dust lifetime from our parametric modeling assuming nominal ages and revised ages from Bell et al. (2013), respectively. The middle panel compares the frequencies to a timescale of 3.25 *Myr* assuming nominal ages. In the right panel, the dotted line shows the predicted curve for a 2.75 *Myr* lifetime to compare with the best-fit value of 5.75 *Myr*.

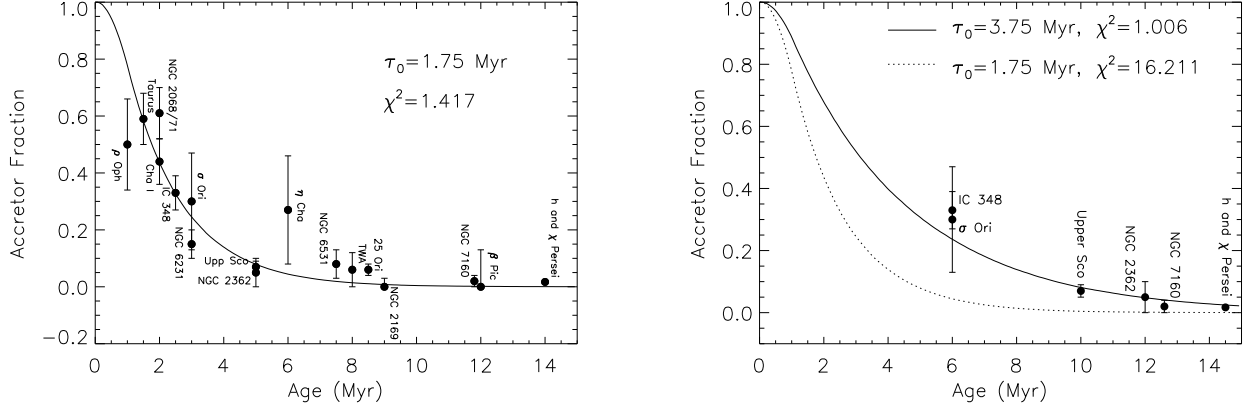


FIG. 16.— Frequency of accreting protoplanetary disks in 1–20 *Myr* old clusters adopting nominal cluster ages (left) and considering revised cluster ages from Bell et al. (2013) (right). The solid lines depict the predicted accretor frequency vs. time for the best-fit curve to the data. The dotted line in the right panel shows the predicted curve for a 1.75 *Myr* lifetime to compare with the best-fit value of 3.75 *Myr*.

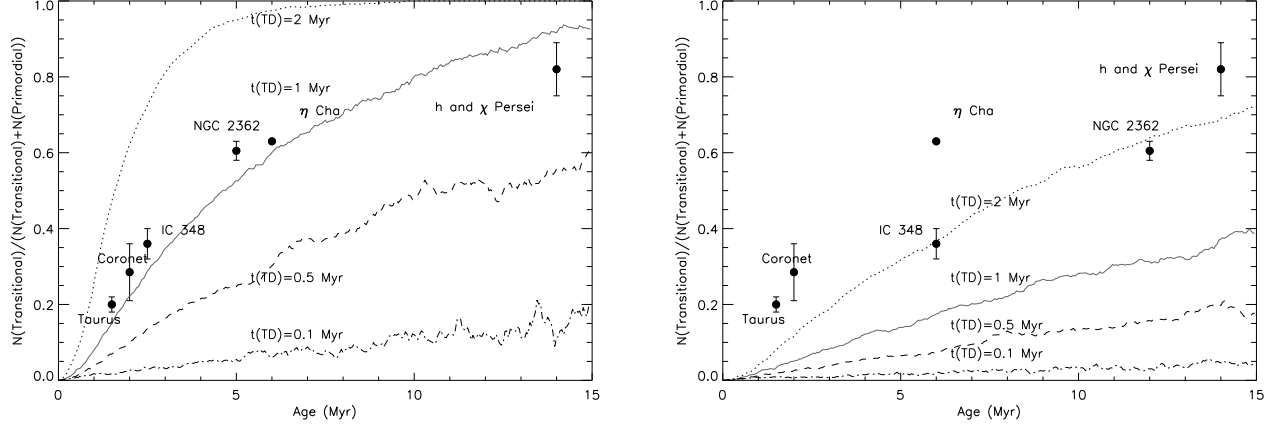


FIG. 17.— The relative frequency of transitional disks vs time in Taurus, the Coronet Cluster, IC 348, NGC 2369, η Cha as in Currie and Sicilia-Aguilar (2011) updated to include h and χ Persei and to consider nominal (left) and revised (right) cluster ages from Bell et al. (2013). For each case, we overplot predicted transitional disk frequencies from our parametric model, adopting a typical proto-planetary disk lifetime of 2.5 Myr (left) and 6 Myr (right). In both cases, the duration of the transitional disk phase is significantly longer than 0.1 Myr and more comparable to ~ 1 Myr.

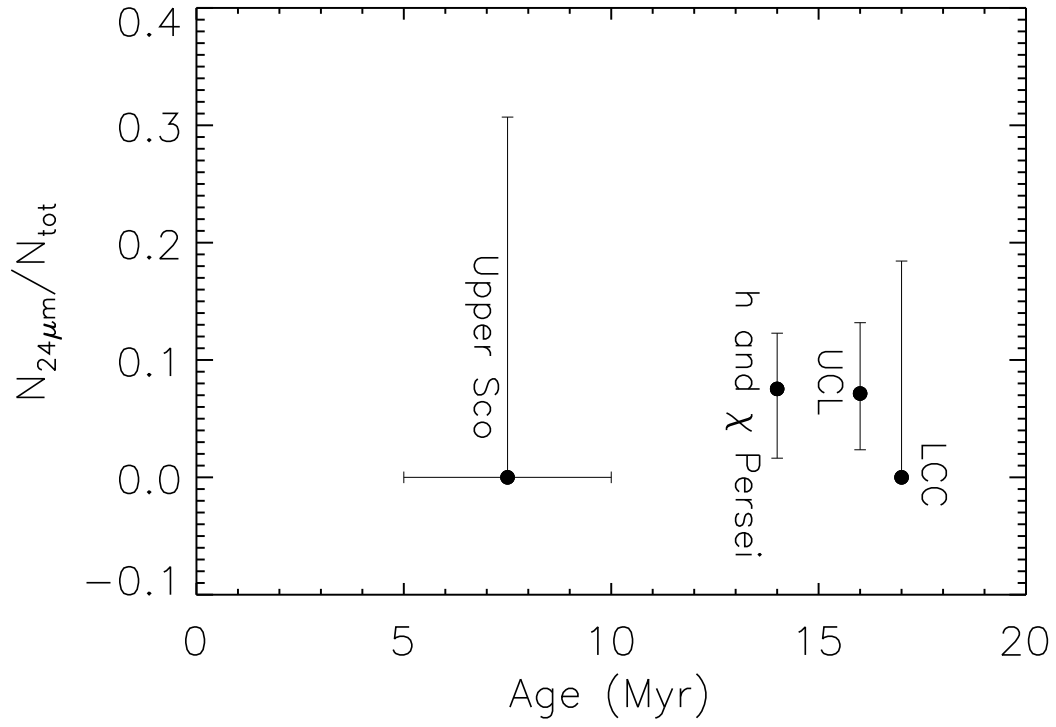


FIG. 18.— Frequency of $24\ \mu\text{m}$ excess emission around $4\text{--}6\ M_{\odot}$ stars h and χ Persei and the the three Sco-Cen subgroups: Upper Scorpius, Lower Centaurus Crux, and Upper Centaurus Lupus.

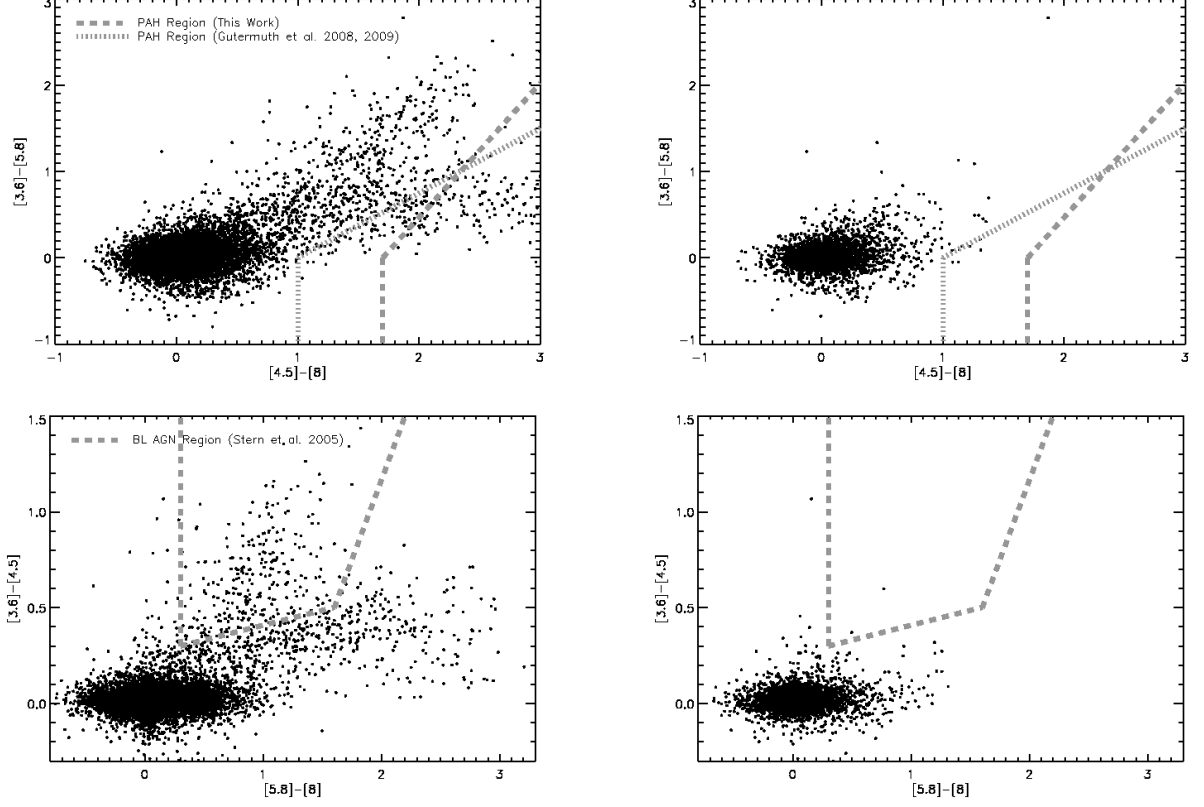


FIG. 19.— $[3.6] - [4.5]$ vs. $[5.8] - [8]$ and $[3.6] - [5.8]$ vs. $[4.5] - [8]$ color-color diagrams for all objects detected in our Spitzer data (left panels) and those previously identified as likely cluster members (right panels) from Currie et al. (2010). The dotted lines enclose the colors typical of active galaxies (Stern et al. 2005; Gutermuth et al. 2008). We do not find evidence for significant residual contamination from active galaxies amongst our sample of Spitzer-detected members.

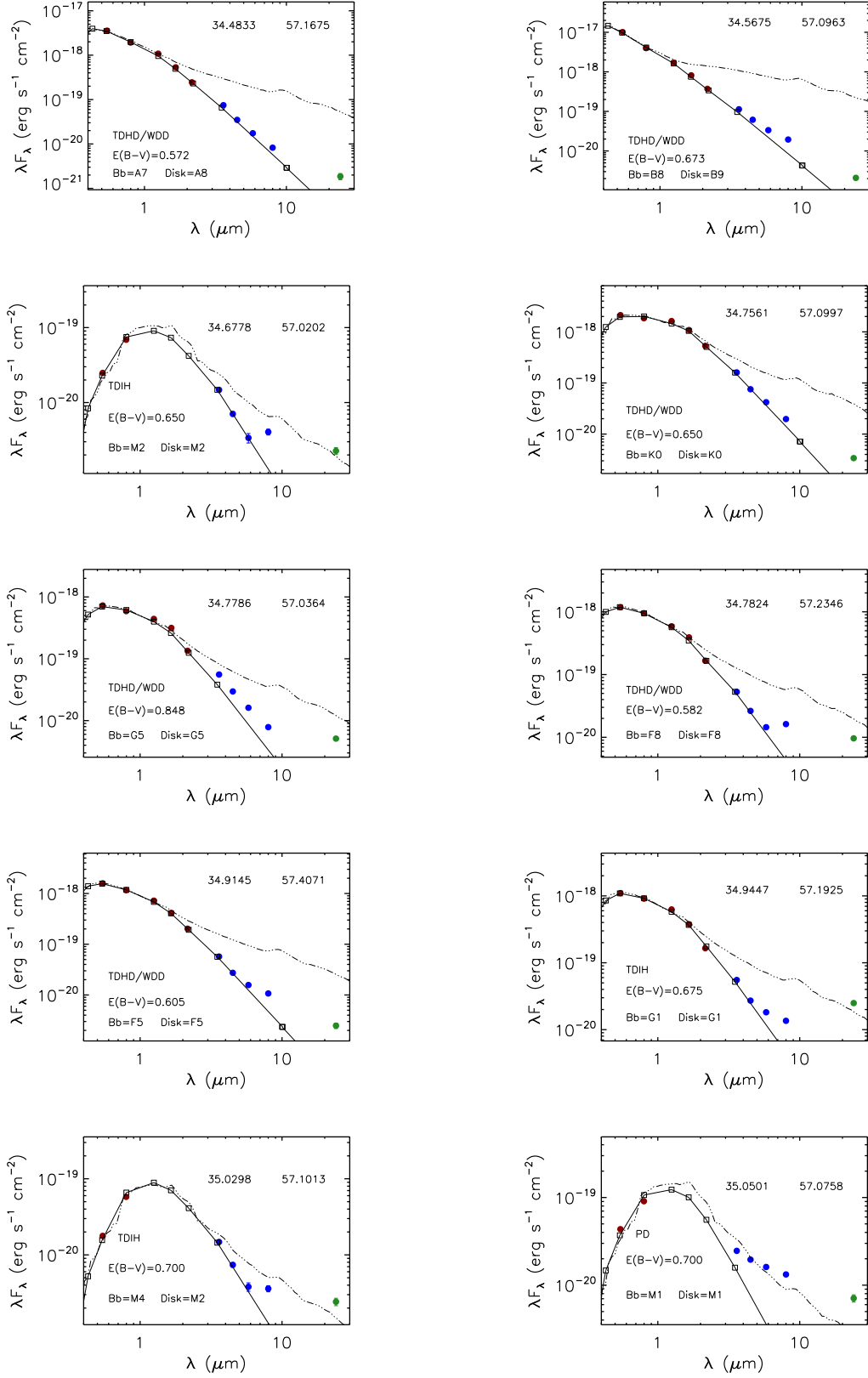


FIG. 20.— Atlas of h and χ Persei stars with clear excesses in IRAC and MIPS bandpasses compared to photometric predictions for a bare stellar photosphere (solid line) and an optically-thick, flat reprocessing disk (dashed line).

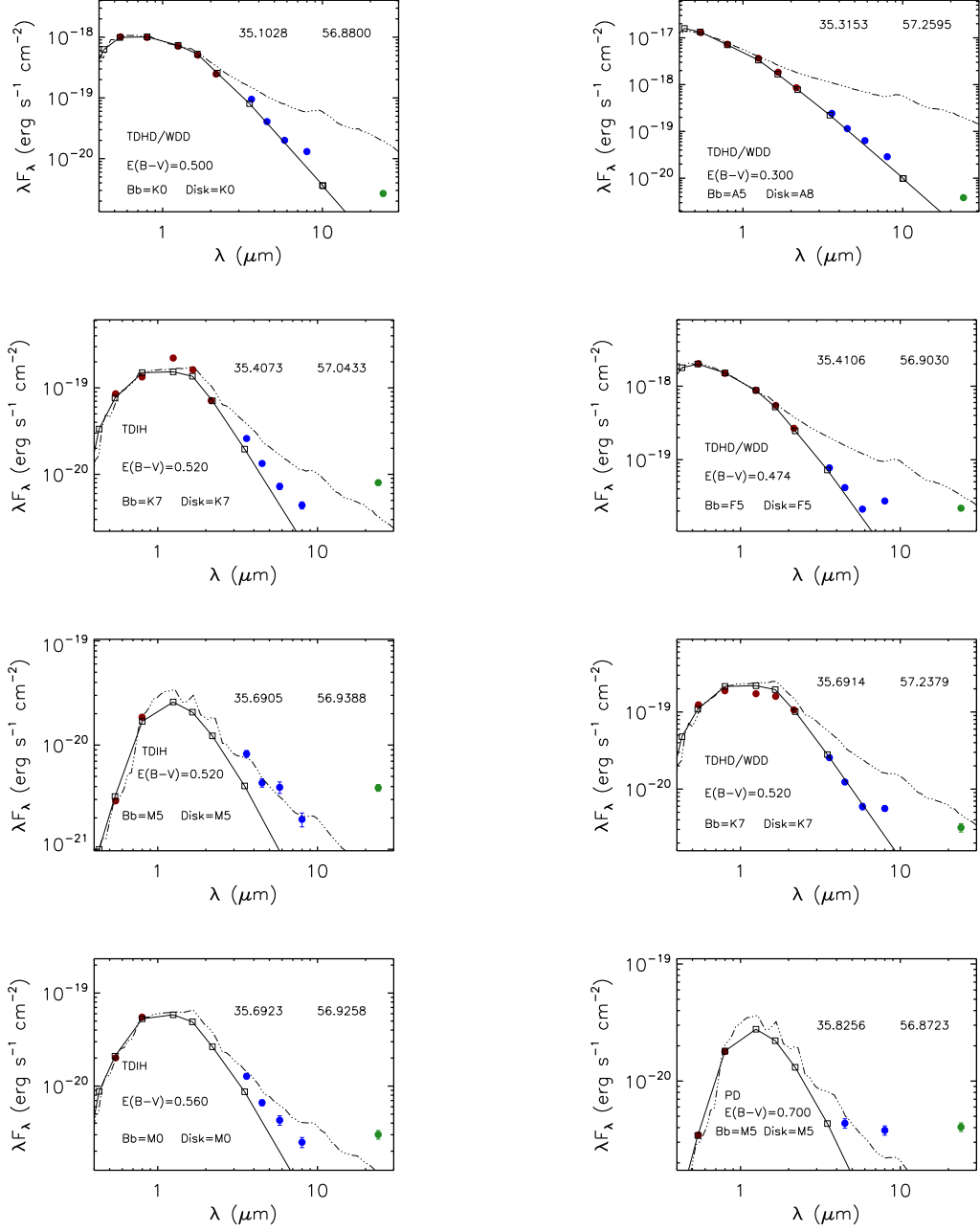


FIG. 21.— Figure 20 continued.